p53 controls choice between apoptotic and non-apoptotic death following DNA damage

Megan E. Honeywell[1], Marie Sophie Lykke Isidor[2], Nicholas W. Harper[1], Rachel E. Fontana[1], Peter Cruz-Gordillo[1], Sydney A. Porto[1], Jessica B. Spinelli[2], David A. Guertin[2], Michael J. Lee[1,2,*]

[1] Department of Systems Biology, UMass Chan Medical School, Worcester, MA, USA

[2] Program in Molecular Medicine, UMass Chan Medical School, Worcester, MA, USA

* To whom correspondence should be addressed: michael.lee@umassmed.edu

SUMMARY

DNA damage can activate apoptotic and non-apoptotic forms of cell death; however, it remains unclear what features dictate which type of cell death is activated. We report that p53 controls the choice between apoptotic and non-apoptotic death following exposure to lethal levels of DNA damage. The canonical response to DNA damage involves p53-dependent activation of cell intrinsic apoptosis, downstream of DNA damage response (DDR) activation. Decades of research suggest that DNA damage does not robustly activate cell death in the absence of p53. In contrast, we find that p53-deficient cells die at high rates following exposure to DNA damage, but exclusively using non-apoptotic types of cell death. Our experimental and computational analyses demonstrate that non-apoptotic death in p53-deficient cells has generally been missed due to use of assays that are either insensitive to cell death, or that specifically measure apoptotic cells. To characterize which subtype of non-apoptotic death is activated by DNA damage in p53-deficient cells, we used functional genetic screening, with an analysis method that enables computational inference of the drug-induced death rate, rather than the relative population size. We find in p53-deficient cells that DNA damage activates a mitochondrial respiration-dependent form of cell death called MPT-driven necrosis. This study reveals how the dual functions of p53 in regulating mitochondrial activity and the DDR combine to facilitate choice between apoptotic and non-apoptotic death following DNA damage.

INTRODUCTION

Understanding the mechanisms of drug action is important for identifying settings in which a drug will be effective, and for interpreting, even predicting, potential mechanisms of drug resistance. For anti-cancer drugs, a key aspect of their mechanism of action is the mechanism by which these drugs promote cell death. The most well-studied form of cell death is apoptosis, and many anti-cancer drugs are known to function by activating apoptotic cell death[1,2]. In recent years, however, more than a dozen non-apoptotic forms of regulated cell death have been identified[3–6]. While these pathways are generally not used in normal development, many non-apoptotic death pathways are valuable therapeutic targets due to their hyperactivation in pathological states, such as in some cancer cells[7]. Furthermore, some anti-cancer drugs can activate both apoptotic and non-apoptotic cell death, but it remains unclear why non-apoptotic death pathways are activated in some contexts but not others[8,9].

The DNA damage response (DDR) is a kinase-driven signaling pathway underlying the efficacy of most conventional chemotherapeutics[10,11]. In addition to recruiting DNA repair machinery, the DDR coordinates the selection of possible downstream cell fates, including cell cycle arrest, permanent senescence, or alternatively, activation of apoptotic cell death. In general, the functional outcome of DDR signaling is dictated by p53. Variations in the dynamics of p53 signaling facilitate the activation of different transcriptional programs, which in turn dictate cell fate[12–15]. While the mechanisms by which p53 signaling and p53 dynamics dictate cell fate choices are becoming increasing understood, it remains unclear how cell fate decisions following DNA damage are regulated in the absence of p53. Furthermore, because p53 is mutated or deleted in most cancers, understanding how p53-deficient cancer cells respond to DNA damage is critical for our understanding of anti-cancer drug action, and our ability to select companion therapies to improve responses.

Most prior studies have found that p53 is required for DNA damage-induced cell death[16–18]. These studies are well-validated and consistently reproducible; however, many DNA damaging chemotherapies are effective in cancers that lack p53. For instance, medullary triple-negative breast cancers universally mutate p53, but paradoxically, these are among the most chemo-sensitive breast cancers[19,20]. Because cell death is generally thought to be required for durable disease remission, and because prior studies have focused exclusively on apoptotic death, we reasoned that other mechanisms must exist to facilitate DNA damage-induced cell death in the absence of p53. Indeed, DNA damage has been demonstrated to activate some forms of non-apoptotic death[21–24], but the mechanisms of activation and the contexts in which apoptotic versus non-apoptotic death would occur remain unclear. Furthermore, because most forms of non-apoptotic death have only recently been recognized, this question remains largely unexplored.

Here we find that p53 is not required for cell death *per se*, but is specifically required for the activation of cell intrinsic apoptosis following DNA damage. Cells die at similar levels following DNA damage with and without p53, but p53-deficient cells preferentially activate a non-apoptotic form of cell death. Using functional genetic screening of single gene knockouts, complemented with a new analysis strategy to infer perturbations to the drug-induced death rate, we find in p53-deficient cells that DNA damage activates a mitochondrial respiration-dependent form of cell death, called MPT-driven necrosis. These findings reveal how the dual functions of p53 in regulating mitochondrial activity and the DDR combine to facilitate choice between apoptotic and non-apoptotic death following DNA damage.

RESULTS

p53 deletion switches the mechanism of cell death following DNA damage from apoptotic to non-apoptotic

Our current understanding of the DNA damage response (DDR) places p53 in a central position, contributing to all downstream functions of the DDR, including DNA repair, cell cycle arrest, and the decision to undergo senescence or apoptotic cell death (Figure 1A)[10]. It is less clear how cell fate decisions following DNA damage are regulated in the absence of p53. To study this issue further, we began by profiling sensitivity to nine commonly used DNA-damaging chemotherapeutics, with each drug tested across a large dose range, in cells containing wild-type p53 (WT) or cells that lack p53 function (KO). We used the FLICK assay (Fluorescence-based and Lysis-dependent Inference of Cell death Kinetics), which enables quantification of the numbers of live and dead cells, and how these populations change over time following drug addition[9,25]. Overall, we found no statistically significant differences in drug sensitivity between p53 WT and p53 KO cell lines (Figure 1B and Supplemental Figure 1A-B). Similar results were found following re-analysis of the DepMap PRISM Repurposing dataset, which contained 90 well-validated DNA damaging agents, each profiled in approximately 500 cell lines (Figure 1C).

A potential issue with interpreting the role of p53 from a meta-analysis performed across drugs and cell lines is that p53 is reported to have functions that vary depending on context. Thus, any critical role for p53 in DNA damage-induced cell death may be washed out by integrating across fundamentally different cellular and drug contexts. Additionally, conventional drug response measurements focus on drug-induced changes in population size. These measurements are confounded by variations in growth rate across cell types, which can obscure underlying differences in drug effects[26,27]. To address these issues and more accurately score how p53 affects cell death following DNA damage, we used the drug GRADE framework to evaluate responses to DNA-damaging chemotherapies[28]. The drug GRADE approach

involves comparison of two complementary measurements: the normalized population growth rate (GR value[26]) and the drug-induced lethal fraction (Figure 1D)[29,30]. These measurements can be used to accurately score the extent to which drugs alter the population growth rate versus the cell death rate.

Within any given cell line, GRADEs for DNA-damaging chemotherapies were generally similar, even across mechanistically distinct classes of DNA damage (Supplemental Figure 1C). However, these scores varied considerably across cell lines, due to cell intrinsic differences in the relative magnitude and coordination of growth inhibitory versus death activating effects of DNA damage. Our GRADE-based analysis revealed that cells lacking p53 grow faster in the presence of DNA damage than cells with functional p53 (Figure 1E and Supplemental Figure 1C). This is perhaps expected, given the role for p53 in facilitating G1-S cell cycle arrest following DNA damage. Surprisingly, however, GRADE-based analysis also revealed that cells lacking functional p53 activate cell death at significantly higher rates than cells with functional p53 (Figure 1E). This is unexpected given numerous studies which demonstrate that p53 is required for DNA damage-induced apoptosis. Thus, GRADE-based analysis reveals hidden and unexpected variation in the DNA damage responses of p53-proficient and p53-deficient cell lines. Furthermore, in contrast to the prevailing model, our data reveal that cells lacking p53 die at high rates following DNA damage.

The insights generated by our GRADE-based evaluation of drug responses are in apparent conflict with the well-validated model that p53 is required for apoptotic cell death following DNA damage. We reasoned that there were at least two possible parsimonious explanations for these unexpected results. First, tumor cells that evolve without functional p53 have higher levels of genome instability and a lower capacity for DNA repair. Thus, these cells may be experiencing higher levels of DNA damage per dose, compared to cells with WT p53. A second possibility could be that cells lacking p53 die primarily via non-apoptotic mechanisms. In the context of DNA damage, the preponderance of published evidence suggests that p53 is not

required for the activation of cell death *per se,* but specifically required for activation of apoptosis[31]. Furthermore, because cell death has typically been evaluated using markers that are specific to apoptotic cells (*e.g.*, caspase-3 cleavage, Annexin V positivity, membrane blebbing), high levels of non-apoptotic death can occur and go unnoticed. To address these issues, we used CRISPR/Cas9-mediated genome editing to knockout p53, facilitating an analysis of p53 function in an isogenic pair of cell lines (Figure 1F). We used U2OS cells, which have wild-type p53 and retain p53-dependent functions, such as p53-dependent G1-S arrest following DNA damage (Supplemental Figure 2A). Loss of p53 did not substantially alter levels of DNA damage, or the duration of DNA damage signaling (Supplemental Figure 2B). To evaluate the role of p53 in DNA damage-induced cell death, we tested the topoisomerase II inhibitor etoposide. We calculated the drug-induced fractional viability (FV, fraction of the population that is alive versus dead), rather than the more conventional “relative viability” (RV, size of the live population compared to untreated). FV is cell death-specific, whereas RV scores both growth and death phenotypes[28]. Etoposide-induced death was similar for U2OS and U2OS^{p53KO}, with the cell death modestly (but significantly) increased in the absence of p53 (Figure 1G). Similarly, acute knockdown of p53 using targeted siRNAs also did not strongly alter the death rate in a panel of genetically diverse cells containing functional p53 (Figure 1H).

While the overall levels of cell death were similar in the presence and absence of p53, evaluating the kinetics of drug-induced cell death revealed clear differences between U2OS and U2OS^{p53KO} cells. In particular, the onset time of cell death in U2OS^{p53KO} was significantly later than in U2OS, but also death occurred at a faster overall rate (Figure 1I). Faster rates of cell death are an indication of increased synchrony of death within the population, which is a common feature of inflammatory non-apoptotic forms of death[30,32–34]. Thus, we also tested whether DNA damage was activating apoptotic or non-apoptotic death in these cells. U2OS and U2OS^{p53KO} cells had equal levels of sensitivity to apoptotic drugs, such as the BH3 mimetic ABT-199 (Supplemental Figure 2C). In response to etoposide, death in U2OS was associated

with the conventional hallmarks of apoptotic death: sensitivity to the caspase inhibitor zVAD, activation of the apoptotic executioner, caspase-3, and acquisition of the characteristic "membrane blebbing" morphology (Figure 1J-L). All of these hallmarks were absent in U2OS^{p53KO}, in spite of the high levels of death induced by DNA damage in these cells (Figure 1J-L). Additionally, conditioned media taken from U2OS^{p53KO} treated with etoposide induced inflammatory responses, which were not observed from conditioned media taken from U2OS cells treated with etoposide (Supplemental Figure 2D-F). Taken together, these data reveal that DNA damage causes similar levels of cell death in the presence and absence of p53, but via distinct mechanisms: cells with functional p53 die via apoptosis, whereas cells without functional p53 die via non-apoptotic mechanisms.

Use of alternative death mechanisms in the absence of p53 has been missed due to assay conditions that are insensitive to cell death

Considering the intense interest in both p53 and cellular responses to DNA damage, we next sought to explore why it had not previously been recognized that DNA damage causes high levels of non-apoptotic death in the absence of p53. It has recently been clarified that variations in the proliferation rate are a common confound when comparing drug sensitivities across different cell types[26,27]. Because p53 regulates both proliferation and cell death, we reasoned that varied growth rates in the presence and/or absence of DNA damage likely contribute to the inability to accurately interpret the extent to which p53 contributes to death following DNA damage. To consider this issue quantitatively, we built a simple model to simulate the population response to DNA damage, focusing on drug-induced changes in relative viability (RV), as RV is overwhelmingly the most common method for evaluating drug responses (Figure 2A). We used this model to quantitatively evaluate the expected changes in RV if p53 controls both the proliferation rate and death rate following DNA damage, or alternatively, if

these phenotypes are uncoupled and p53 regulates the proliferation rate but not the death rate, as we see in our empiric analysis.

To begin, we parameterized our model using growth rates and death rates observed in using our GRADE-based analysis (Figure 1 and Supplemental Figure 2G). In the presence of p53, DNA damage induces a bi-phasic response, characterized by growth inhibition at low doses, and cell death occurring only at higher doses and only in non-proliferative cells[28,35]. As a result, the death rate that we observe following high levels of DNA damage is surprisingly low, and would not be sufficient to shrink a tumor population, if the tumor cells were not also growth arrested. Intuitively, our simulations revealed that loss of either p53-dependent growth inhibition or p53-dependent death activation should result in a similar qualitative phenotype of increased RV, with full rescue to untreated levels requiring loss of both the growth inhibiting and death activating functions of p53 (Figure 2B). Importantly, a more quantitative analysis of population size reveals that relative viability is ostensibly an evaluation of the drug induced-growth rate, as the presence or absence of drug-induced cell death does not strongly alter the overall population size, particularly when measured after long durations of drug exposure that are typically used in drug response evaluation (Figure 2B-C). Thus, due to common drug response measurements and commonly used assay times, the degree to which p53 does- or does not contribute to the death rate following DNA damage is not easily observed.

Increased relative viability is often interpreted as increased cell survival. This interpretation is well-accepted, particularly if increased relative viability is also associated with loss of observable dead cells. Another issue that contributes to under-scoring non-apoptotic death is that cell death is typically evaluated using markers that are specific to apoptotic cells, such as caspase-3 cleavage or Annexin V positivity. Our evaluations of cell death were made using an assay that depends on SYTOX fluorescence, which is specific to dead cells but agnostic to the mechanism of cell death[9,25]. Thus, the non-apoptotic death that occurs following

DNA damage will typically be missed by death assays that rely on intact cellularity and acquisition of apoptotic hallmarks.

Genetic screens fail to identify death regulatory proteins due to the confounding effect of varied growth rates

Having found that cells lacking p53 die predominantly using non-apoptotic mechanisms following DNA damage, we next sought to determine which form of non-apoptotic death was being activated. At least 15 mechanistically distinct subtypes of cell death have been characterized, most of which induce a morphologically necrotic form of death[3–6,36]. We began by evaluating eight pathways, for which we had well-validated inhibitors that were functional in inhibiting the canonical activator of each pathway. Each single pathway inhibitor failed to inhibit the lethality of etoposide in U2OS^{p53KO} cells, as did higher order combinations of these inhibitors (Supplemental Figure 3). Thus, in the absence of p53 it appears that death following DNA damage occurs using either a poorly characterized form of cell death, or a combination of death subtypes that we were unable to evaluate using chemical inhibitors.

Genome-wide knockout screening has been successfully used to reveal genetic dependencies for a variety of phenotypes[37]. When performed in the context of drugs, “chemo-genetic” profiles are useful for inferring mechanisms of drug action, and potentially also the mechanisms of cell death[38,39]. To reveal mechanisms of cell death in the presence and absence of p53, we used the GeCKOv2 sgRNA library to generate single gene knockouts across the full genome, in Cas9-expressing U2OS or U2OS^{p53KO} cells (Figure 3A)[40]. We focused on the topoisomerase II inhibitor etoposide, which induced apoptotic death in U2OS and non-apoptotic death in U2OS^{p53KO} cells. In most prior studies, drugs have been screened at doses that confer 20-50% reductions in population size over 2-4 weeks (*e.g.*, “ED20” or “ED50” dose)[41]. For DNA damaging drugs, however, we observed that all doses less than “ED95” fail to induce any cell

death (Supplemental Figure 4A-B). Thus, the conventional screening parameters would likely fail to identify cell death regulatory genes.

To optimize our screen for evaluation of cell death, we shortened the assay time, such that evolution of the sgRNA population would be driven primarily by variations in the degree of cell death between clones, rather than by variations in the degree of proliferation. Treatment with 5 μM etoposide for 4 days resulted in ~50% lethal fraction in both cell types (Figure 3B). Furthermore, because cells at this dose continued to proliferate for the first ~24 hours after drug exposure, high levels of cell death could be obtained without causing a population “bottleneck”, which would deteriorate assay sensitivity (Figure 3C). In our screens, we recovered 99.9% of all sgRNAs covering 100% of all genes in every replicate, and our biological replicates were highly correlated, both in terms of counts and gene effect (Supplemental Figure 4C-E). Furthermore, known essential genes were already becoming depleted in the comparison of endpoint versus “T0” samples, even at the early time points selected in our screen (Figure 3D). Taken together, these data suggest that the quality of our data were not compromised by the atypical assay conditions and high levels of drug-induced death used in our screen.

Functional genetic screens using pooled libraries are typically analyzed by computing the relative growth fitness of each knockout. Guide-level or gene-level fitness scores are computed by comparing the relative abundance of guides or genes between the drug-treated and untreated conditions. Notably, the comparison of drug-treated versus untreated is precisely the same as “relative viability”, the most common drug response metric. Because RV-based measurements failed to accurately capture the contribution of cell death, we reasoned that it was predestined that our screen would fail to identify death regulatory genes if analyzed in the conventional manner. To explore this logic, we analyzed our screen using a conventional comparison of treated versus untreated groups. We focused on U2OS cells, where etoposide induced apoptotic death, as apoptotic regulatory genes are well described. As we expected, genes that regulate apoptosis did not score as significantly enriched or depleted in our screen;

instead, analysis approaches focused on scoring the fold change between treated and untreated populations primarily identified genes that regulate cell proliferation (Figure 3E). To explore whether this is a common issue, we performed a meta-analysis of previously published screens of known apoptotic drugs. Of the 74 screens that we re-analyzed, none were effective in enriching for hallmark apoptotic genes, but these screens in general were effective in enriching for genes that regulate proliferation (Figure 3F). Thus, common analysis methods used for chemo-genetic profiling are insensitive to death regulatory genes.

In the context of RV-based analysis of drug sensitivity, a critical issue is the confounding influence of growth rate variation, particularly when comparisons are made between cell types with different growth rates[26,42]. The confounding influence of growth rate variation can also clearly be observed in our population fold change-based chemo-genetic profile. For instance, U2OS and U2OS^{p53KO} cells have unexpectedly similar genetic sensitivities, given that etoposide induces different forms of death in these two cell types (Figure 3G). Thus, the death mechanism was not a dominant contributor to the chemo-genetic profiles when analyzed using a relative population size metric. Further inspection also revealed that genes whose knockout induced drug sensitization or resistance often scored in an unexpected or paradoxical direction. For example, knockout of genes involved in repairing etoposide-induced DNA damage should phenocopy higher doses of etoposide, and thus should sensitize cells to etoposide (*e.g.,* negative L2FC). Empirically, we observe that knockout of DNA repair genes causes increased L2FC, which is commonly interpreted as promoting drug resistance (Figure 3G). In this context, we reasoned that the inverted phenotype likely did not result from increased survival in the treated population, but rather from decreased growth rate in the untreated population relative to wildtype cells. To further validate this insight, we also looked at core essential genes, which drop out over time due to low growth rates[43]. These genes also score as inducing resistance to etoposide when knocked out (Figure 3G). Thus, as with *in vitro* drug response analysis, growth

rate variation between clones confounds the interpretation of pooled genetic screens, limiting the ability to identify mechanisms of death regulation.

Death rate-based analysis accurately identifies genes that regulate drug-induced death

Based on our meta-analysis of published data, it was clear that accurately identifying death regulatory genes from our chemo-genetic profiling data would require a calculation of the drug-induced death rate, rather than the relative population size or relative growth fitness. For *in vitro* drug response analyses, accurate calculation of the death rate requires counting both the live and dead cell fractions[28,30]. Recovery of dead cells is possible in the context of apoptotic death due to the relative stability of the apoptotic corpse, and this approach has been applied to chemo-genetic profiling[44,45]. However, recovering intact dead cells is likely not possible in the context of non-apoptotic death due to cell rupture. Thus, we next sought to develop a new computational method to infer the death rate from the data that is typically available in chemo-genetic profiling studies. To explore how to achieve this, we began by developing a simple model of population dynamics in the presence and absence of DNA damage (Figure 4A). Growth and death rates for our model were parameterized based on drug titration data used to optimize our screen (Figure 2C). Using this model, we simulated all possible combinations of growth rates and drug-induced death rates, treating these features as independent variables. From the simulated data, we computed the relative size of the treated and untreated populations, as is conventionally done in fold change-based analysis of chemo-genetic profiles. The results of this comprehensive simulation revealed with more clarity the nature of the confounding influence of growth rate variation: it is possible to accurately interpret the direction and magnitude of each gene deletion's effect on cell death, but only if the gene deletion does not result in a growth rate perturbation (Figure 4B). For each single gene knockout, as the growth rate in the untreated condition is decreased from the wild-type growth rate, the inference of the gene's function in the treated condition is compromised, even inverted if the growth defect

is strong enough (Figure 4C). To confirm that slow growth in the untreated condition was responsible for the inverted inference of DNA repair genes, we calculated the growth fitness defect for DNA repair genes in the untreated condition compared to the initial “T0” sample. These data revealed that knocking out DNA repair genes significantly compromises the growth rate of cells, even in the absence of external DNA damage (Figure 4D).

Our simulation also revealed a straight-forward strategy for inferring the drug-induced death rates from our existing data. The central issue is that the population size at assay endpoint is not proportional to the drug-induced death rate, but rather, is a function of the genetic- and drug-induced changes to both growth and death rates. In the context of the high levels of DNA damage screened in our assay, death only occurs in growth arrested cells (Supplemental Figure 5A)[28]. The lack of growth during the death phase of the response significantly simplifies the possible ways that perturbations to growth rate and death rate integrate to create a given number of cells. Thus, the varied combinations of growth rates and death rates that yield the same population size create a single continuous non-linear “manifold” at each level of L2FC (Supplemental Figure 5B). The implication of this simple structure is that the drug-induced death rate for each single gene knockout can be clearly inferred from a combination of the relative population size (*e.g.*, L2FC) and the relative growth rate in the absence of drug (*e.g.*, the gene fitness score when comparing untreated to T0) (Supplemental Figure 5C). Using this inference approach, we computed the gene-level growth rates and death rates for each single gene knockout. We projected these data into the phase diagram generated from our simulation (Figure 4E). This analysis revealed, as anticipated, that knocking out DNA repair genes increases the death rate of cells exposed to DNA damage (*e.g.*, positive values on the y-axis), but that this phenotype is not apparent due to the slow growth rate of these cells in the untreated condition (*i.e.,* Type III error, Figure 4C and E). The slowed growth rate and increased death rate integrate in a manner that leads to enrichment of these cells in the treated

condition when compared to the untreated population (*e.g.*, accumulation in the red portion of the diagram).

Our analysis also identified “false negatives” (*i.e.*, Type II error) that could be rescued by our death rate analysis. For instance, TDP2 is a DNA repair protein that specifically repairs adducts created by drugs like etoposide[46]. Thus, knocking out TDP2 is well-validated to increase etoposide potency[41]. A conventional L2FC-based analysis scores TDP2 at approximately 0, suggesting that knocking out TDP2 had no effect on etoposide sensitivity. Alternatively, our death rate analysis suggests that the neutral L2FC results from a combination of increased death rate in the drug-treated condition and decreased growth rate in the untreated condition. To validate these model-inferred predictions, we tested TDP2-targeting sgRNAs from the GeCKOv2 library for their effect on both cell proliferation and cell death. Confirming our model-inferred predictions, sgRNA-mediated knockout of TDP2 resulted in a slower growth rate in the absence of exogenous DNA damage, and a faster death rate in the presence of etoposide (Figure 4F).

The model we use to infer the drug-induced death rate relies on a critical assumption, that the cell death occurs following DNA damage in a non-growing population. While this assumption is experimentally validated for wild-type cells, it may not always be true in the context of single gene deletions which could alter the coordination of growth and death. Thus, we performed a large-scale validation of our death rate inferences for different classes of predictions (Figure 4G and Supplemental Figure 5D-E). We focused on the top 20 genes predicted to increase or decrease the death rate using our inference approach. For comparison, we also evaluated the top 20 genes predicted to cause drug sensitization or drug resistance based on more conventional L2FC-based analysis methods. In total, 40 genes were evaluated in an arrayed format using the FLICK assay to score the population death rate following exposure to etoposide. Overall, death rate-based analysis of our chemo-genetic profiling data was strongly predictive of the death regulatory function of each gene (Figure 4H).

For the traditional analysis methods, our chemo-genetic profiling data was not significant for predicting the cell death regulatory function of the 40 tested genes (Figure 4I). The data, however, were also clearly non-random (OR = 6.6) and may have been significant if we tested a larger set of genes. We note, however, that these two analysis methods only produce conflicting predictions for gene knockouts that cause reduced growth rates. Thus, to directly compare rate-based and population fold-change-bases analyses, we focused on the subset of genes whose deletion caused a reduced growth rate. For gene knockouts that result in slow growth, death rate-based analysis predicts divergent phenotypes, whereas fold-change analysis uniformly predicts drug resistance due to the confounding influence of slow growth rate (Supplemental Figure 5F). Regardless of the growth rate, death rate-based analysis continues to accurately predict the death regulatory function of each gene (Figure 4J). Importantly, for gene knockouts with a reduced growth rate, a population fold-change analysis produced worse than random predictions of the cell death regulatory function (Figure 4J). Taken together, these data reveal that commonly used analysis methods are insensitive and inaccurate for studying cell death, and that a death rate-based analysis can improve the accuracy and interpretation of the death regulatory function of genes.

In the absence of p53 DNA damage activates a mitochondrial respiration-dependent form of necrosis

We next sought to determine if our death rate data were sufficient for interpreting mechanisms of drug-induced cell death, and if these data could be used to determine which mechanism of cell death is activated by DNA damage in the absence of functional p53. Our chemo-genetic profile identified 502 genes that modulate death rate when deleted in wild-type U2OS, and 755 genes that modulate the etoposide-induced death rate when deleted in U2OS^{p53KO} cells. Importantly, the overwhelming majority of these “hits” were observed in only one of the two genetic contexts (*e.g.*, 619 of 755 genes were unique to U2OS^{p53KO} cells); and

overall, we observed a poor correlation between the death rates in the presence and absence of p53 (Figure 5A). This is in stark contrast to what we observed with a conventional fold change-based analysis, in which scores were similar for p53 WT and KO cells (Figure 3G). Additionally, many expected phenotypes were observed with the correct directionality in our death rate analysis. For instance, deletion of p53, or critical p53-target genes such as p21 (CDKN1A), increased the death rate exclusively in the p53 WT background, whereas deletion of critical DNA repair factors such as TDP2 increased the death rate in both backgrounds (Figure 5A).

To determine if these data are sufficient for interpreting the mechanism of cell death activated by etoposide, we focused first on U2OS cells, where death occurs via canonical apoptosis. Importantly, in U2OS, gene deletions that alter death rate were significantly enriched for known apoptotic regulatory genes (Figure 5B). These effects were not observed in the U2OS^{p53KO} background. Furthermore, the distinction between p53-proficient and p53-deficient cells was not observed when we used a conventional fold change-based analysis (Figure 5B). These data further confirm a lack of DNA damage-induced apoptosis in p53 KO cells, and the unique sensitivity of our death rate-based analysis method for revealing the mechanism of cell death.

Most non-apoptotic death subtypes remain poorly annotated, but in general, for each death subtype at least some unique effector enzymes are known[3]. To determine the mechanism of cell death activated by etoposide in the absence of p53, we began by identifying genes/genetic signatures that were enriched in etoposide treated U2OS^{p53KO} cells, and which were not also observed U2OS. This analysis revealed a unique dependency in U2OS^{p53KO} cells for genes involved in oxidative phosphorylation (OXPHOS) (Figure 5C-D). Deletion of OXPHOS regulatory genes rescued viability in etoposide-treated U2OS^{p53KO}; however, knocking out these genes had no effect in U2OS (Figure 5E).

OXPHOS regulatory proteins are components of a mitochondrial respiration-dependent form of cell death called mitochondrial permeability transition (MPT)-driven necrosis[3,47]. MPT-

driven necrosis is thought to be caused by opening of a mitochondrial permeability transition pore (mPTP), loss of mitochondrial inner membrane integrity, and mitochondrial rupture. These events ultimately cause a morphologically necrotic death. Many of the molecular and mechanistic details of MPT-driven necrosis remain unknown and/or controversial; however, it is well-established that MPT-driven necrosis depends on the activity of cylcophilin D (CYPD; MPT-driven necrosis is also known as CYPD-dependent necrosis)[48]. CYPD-dependent death is generally evaluated using the cyclophilin family inhibitor, cyclosporin A (CsA)[47,49]. In our initial evaluation of non-apoptotic death pathways, we did not evaluate MPT-driven necrosis, as CsA itself activated apoptotic death in U2OS cells (Supplemental Figure 6A). To more carefully evaluate whether MPT-driven necrosis contributes to DNA damage-induced cell death in the absence of p53, we tested CsA in combination with the apoptotic inhibitor zVAD. As expected, zVAD neutralized the lethality of CsA, and the combination of these inhibitors did not affect the fitness or viability of cells in the absence of drug exposure (Supplemental Figure 6B). In the presence of zVAD, CsA slowed the onset of etoposide-induced death in U2OS^{p53KO} cells, but did not affect the etoposide response in U2OS (Figure 5F). Additionally, we tested inhibitors of other necrotic pathways for which mitochondrial activity contributes to lethality. None of these inhibited death in U2OS^{p53KO} cells (Figure 5F).

To further evaluate whether MPT-driven necrosis is activated by DNA damage in the absence of p53, we sought to monitor opening of the mitochondrial permeability transition pore (mPTP). We used the Co2+-calcein assay, in which cytoplasmic fluorescence of calcein is quenched by cobalt, which cannot enter the mitochondrial matrix; opening of the mPTP facilitates cobalt entry and quenching of mitochondrial calcein fluorescence[50]. In U2OS^{p53KO} cells etoposide exposure caused a significant decrease in mitochondrial calcein fluorescence (Figure 5G-I). Similar results were found in a larger panel of p53-deficient cell lines, with mitochondrial calcein fluorescence being lost following exposure to a lethal dose of etoposide (Supplemental Figure 6C). In U2OS cells which die by apoptosis, we observed no change in mitochondrial

calcein fluorescence following exposure to etoposide (Figure 5G-I). Taken together, these data demonstrate that DNA damage activates MPT-driven necrosis in the absence of p53.

DISCUSSION

In this study, we describe a previously uncharacterized function for p53 in biasing how cells respond to lethal levels of DNA damage. It has long been known that p53 is required for robust activation of apoptosis following DNA damage, but prior studies have generally concluded that loss of p53 promotes cell survival following DNA damage. In contrast, in cancer cells that are naturally deficient for p53 and in cells genetically engineered to lack p53, we find that loss of p53 does not decrease the levels of DNA damage-induced cell death. Instead, cells lacking p53 simply die using a non-apoptotic form of cell death. Our loss of function genetic screening and mitochondrial activity profiling reveal that a dominant form of DNA damage-induced cell death in p53-deficient cells is MPT-driven necrosis.

Some prior studies have also found that p53-deficient cells can use other pathways to activate apoptotic cell death, such as a caspase-2-dependent signaling pathway that is inhibited by Chk1[51]. Our prior studies have revealed a phenomenon that is commonly observed in the context of cell death called “single agent dominance”, in which faster acting death pathways suppress the activation of slower acting pathways[9]. Thus, while other forms of death were not observed in the panel of p53-deficient cell types used in this study, this potential variation highlights that many different types of death may be possible once the canonical cell intrinsic apoptotic response is no longer a dominant mechanism. Nonetheless, our study suggests that MPT-driven necrosis is the dominant form of cell death in DNA damaged cells that lack functional p53. Furthermore, as we highlighted in this study, the non-apoptotic form of death that we found would likely not have been observable in prior studies due to the use of common use assays that are either biased towards proliferative effects, or specifically measurements of

features of the apoptotic corpse. These findings highlight that studies of anti-cancer drug responses should include either direct measurements of each relevant form of cell death, or death-specific measurements that are agnostic to the type of death, with the precise death mechanism inferred through genetic and chemical dependencies, as in this study.

Additionally, a surprising observation from this study has been that pooled loss of function genetic screens are systematically biased against cell death regulatory genes. Intuitively, growth fitness (*i.e.,* the relative population growth rate) is influenced by changes to both the cell proliferation rate and the death rate. Thus, functional genetic screens should, in principle, be sensitive to knockout of death regulatory genes. The modeling and analysis in this study reveals three culprits for the common lack of sensitivity to death regulatory genes that has been observed in functional genomic studies: use of non-lethal drug concentrations, use of long assay lengths that bias towards proliferative phenotypes, and use of analytical methods that fail to address the confounding effects of growth rate variation in the untreated samples.

Growth rate variation has similarly been recognized as a confounding influence in the evaluation of drug sensitivity. In the context of *in vitro* drug sensitivity evaluation, the drug-induced death rate can be accurately scored by measuring both the live and dead cell populations. Because it is often not possible to make these measurements for non-apoptotic death, we generated a new method for inferring the drug-induced death rate from a combination of three insights: 1) the population size at assay end point, 2) the experimentally measured growth rate for each clone in the pool, and 3) the known mechanisms coordination of growth and death from GRADE-based analysis. While the model we used for our analysis was specific for the growth-death coordination that is observed for DNA damage, with appropriate modifications to this model, these methods should be usable in any other drug context. Moreover, while other methods, such as direct sequencing of dead cells following sorting, can be effective in the context of apoptotic death, the methods used in this study are likely to be the best methods for evaluating non-apoptotic types of death.

Taken together, our findings also reveal that the methods used throughout the community for evaluating drug sensitivity have generated a systematic bias, limiting our understanding of non-apoptotic forms of cell death. In the context of p53-deficient cancers, we found unexpectedly high levels of non-apoptotic death following DNA damage. Because necrotic cells are difficult to recover and because these cells lack the conventional hallmarks of apoptotic cells, non-apoptotic death can go undetected, and the phenotypes would previously have been erroneously attributed to lack of proliferation. As we report herein, the genetic dependencies for apoptotic and non-apoptotic forms of cell death are distinct, even when death is activated by a common stimuli, like etoposide-induced DNA damage. Thus, efforts to personalize lethal drug therapies would likely benefit from understanding the shared versus death pathway-specific genetic dependencies for commonly used therapeutic agents. The extent to which targeting non-apoptotic death pathways in p53-deficient cancers would improve therapeutic responses remains to be determined, but our studies reveal the prominent use of MPT-driven necrosis in p53-deficient cancers, and the genetic determinants for DNA damage-induced and MPT-driven cell death.

METHODS

Cell lines and reagents

A431, A549, BT549, HCC1143, HCC1806, HT-29, MCF7, MCF10A, MDA-MB-231, MDA-MB-436, MDA-MB-453, MDA-MB-468, SK-BR-3, and U2OS cells were obtained from the American Type Culture Collection (ATCC). A375, HT-1080, Malme-3M, NCI-H460, and UACC62 cells were acquired from the Green lab (UMass Chan Medical School). Caki-1 cells were a acquired from the Kim lab (UMass Chan Medical School). A375, A431, A549, MCF7, MDA-MB-231, MDA-MB-436, MDA-MB-453, MDA-MB-468, and U2OS cells were grown in DMEM (Corning, #10-017-CV). HT-1080 cells were grown in EMEM (ATCC, #30-2003). Malme-3M cells were grown in IMDM (Thermo Fisher Scientific, #12440053). Caki-1, HT-29, and SK-BR-3 cells were grown in McCoy's 5A medium (Corning, #10-050-CV). BT549, HCC1143, HCC1806, NCI-H460, and UACC62 cells were grown in RPMI 1640 medium (Corning, #10-040-CV). MCF10A cells were grown in DMEM-F12 medium (Thermo Fisher Scientific, #11320033) supplemented with 5% horse serum, 20 ng/ml epidermal growth factor (EGF), 0.5 mg/ml hydrocortisone, 100 ng/ml cholera toxin (Sigma-Aldrich, #C8052-2MG), 10 µg/ml insulin (Life Technologies, #12585014), and penicillin-streptomycin (Corning, #30-002-CI). Each media (except DMEM-F12) was supplemented with 10% fetal bovine serum (Peak Serum, #PS-FB2, Lot #21E1202), 2 mM glutamine (Corning, #25-005-CI), and penicillin/streptomycin (Corning, #30-002-CI).

SYTOX Green (#S7020) and LIVE/DEAD Fixable Violet Dead Cell Stain (#L34964) were purchased from Thermo Fisher Scientific. p53 mouse antibody (#48818) and p-H2A.X rabbit antibody (#9718) were purchased from Cell Signaling Technologies. β-Actin mouse antibody (#A2228) and actin rabbit antibody (#A2066) were purchased from Sigma-Aldrich. Anti-Active Caspase-3 antibody (#559565) and Anti-Cleaved PARP-647 (#558710) were obtained from BD Pharmingen. Goat anti-rabbit Alexa-488 secondary antibody (#A-11008) was purchased from

Thermo Fisher Scientific. Anti-phospho-Histone H3 rabbit antibody (#06-570) and propidium iodide (#81845) were purchased from MilliporeSigma. Camptothecin (#S1288), Carboplatin (#S1215), Chlorambucil (#S4288), Cisplatin (#S1166), Idarubicin HCl (#S1228), Irinotecan (#S2217), Etoposide (#S1225), Ferrostatin-1 (#S7243), Necrostatin-1 (#S8037), Nutlin-3 (#S1061), Rucaparib (#S1098), Teniposide (#S1787), and Topotecan HCl (#B2296) were purchased from Selleck Chemicals. ABT-199 (#A8194), E 64D (#A1903), Hydroxychloroquine Sulfate (#B4874), VX-765 (#A8238), Z-IETD-FMK (#B3232), and Z-VAD-FMK (#A1902) were purchased from APExBIO. Cyclosporin A (#30024) was obtained from Sigma-Aldrich. Blasticidin (#BP264750) was bought from Fisher Scientific, and Puromycin (#61-385-RA) was purchased from Corning. Pooled siGENOME siRNAs were purchased from Dharmacon/Horizon Discovery. The non-targeting siRNA pool (#D-001206-13-05) contains sequences UAGCGACUAAACACAUCAA, UAAGGCUAUGAAGAGAUAC, AUGUAUUGGCCUGUAUUAG, and AUGAACGUGAAUUGCUCAA. Pooled siRNAs against p53 (#M-003329-03-0005) include the sequences GAGGUUGGCUCUGACUGUA, GCACAGAGGAAGAGAAUCU, GAAGAAACCACUGGAUGGA, and GCUUCGAGAUGUUCCGAGA.

Immunoblotting

Lysates for immunoblotting were prepared from cells seeded in either 6-well plates (200,000 cells per well) or 10 cm dishes ($1.5x10^6$ cells per dish). Cells were adhered overnight and then drugged the following morning ("T0"). At each of the indicated timepoints, media was removed from each sample and collected in a conical tube. Samples were washed with PBS, which was collected in the same conical tube. Cells were then trypsinized and pelleted together with their corresponding media/PBS wash. SDS-lysis buffer (50 mM Tris-HCl, 2% SDS, 5% glycerol, 5 mM EDTA, 1 mM NaF, 10 mM β-glycerophosphate, 1 mM PMSF, 1 mM Na_3VO_4, protease inhibitor and phosphatase inhibitor tablet) was used to lyse the cell pellets. Centrifugation through a 0.2 µm multi-well filter plate (Pall Laboratory, #5053) was used to

remove DNA from the lysates. The protein concentration of each sample was quantified with a BCA assay (Thermo Fisher Scientific, #23225). Lysates were normalized to the same protein concentration and run on precast 48-well E-PAGE gels (Thermo Fisher Scientific, #EP04808). Gels were transferred to nitrocellulose membranes using the iBlot semidry system (Invitrogen) and then blocked for 1 hour in 50% PBS : 50% Odyssey Blocking Buffer (OBB, LI-COR Odyssey, #927-40010). Membranes were incubated overnight at 4°C in primary antibody (diluted in 50% PBS-T (PBS + 0.1% Tween-20) : 50% OBB), and then stained with infrared dye-conjugated secondary antibodies (LI-COR). A LI-COR Odyssey CLx scanner was used to visualize the immunoblots.

Evaluation of p53 function

For our re-analysis of public data, we divided cell lines into p53-proficient and p53-deficient groups based on their DepMap annotated sensitivities to MDM2 deletion. MDM2 inhibition causes a proliferation defect only for cells that retain p53 function[52]. For this reason, MDM2 deletion scores as “essential” in screens of p53 WT cells. Based on this analysis, we identified 90 cell lines that have functional p53, and 305 cell lines in which p53 is non-functional. This classification was used to determine the DNA damage sensitivity of p53 WT and p53 KO cells lines from DepMap. The drug sensitivity data used was the PRISM Repurposing Primary Screen, version 19Q4. This data comes from a multiplexed cell-line viability assay that was used to evaluate a large panel of small molecules. Each cell line in the dataset was bifurcated by p53 status, and drugs whose mechanism of action is DNA damage were identified. The distribution of PRISM fold-change scores for these drugs was plotted as a violin in Prism 9.

Functionality of p53 in our isogenic cell lines was assessed with two complementary methods. First, expression of p53 was measured using a western blot. Stabilization of p53 was induced by treating cells with 10 μM Camptothecin for 2 hours, and immunoblotting was performed with an antibody against p53. Second, flow cytometry was used to determine the

functionality of p53. U2OS cells and U2OS^{p53KO} clones were treated with 10 μM Nutlin-3 for 24 hours, and stained with PI and pH-H3 antibody (described in detail below). Measurement of cell cycle position and cell cycle arrest was performed in FlowJo, and cells without p53-dependent G1 and G2 checkpoints were classified as p53-deficient (KO).

Generation of U2OS^{p53KO}

U2OS^{p53KO} cells were generated in two steps. First, U2OS cells were transduced with virus containing lentiCas9-Blast (Addgene, #52962). Cells were then treated with 5 μg/mL blasticidin for 5 days to make a stable population of U2OS-Cas9 cells. A gRNA cloning vector (Addgene, #41824) was then used to knock out p53. The synthesis protocol provided by the Church lab (available on Addgene) was followed to generate a plasmid with an sgRNA against p53 (5'GATCCACTCACAGTTTCCAT'3). The p53-sgRNA plasmid was transiently transfected into U2OS-Cas9 cells using Lipofectamine 2000 (Thermo Fisher Scientific, #11668027). The transfected cells were then treated with 10 μM Nutlin-3 for 7 days to enrich for p53 KO cells. Nutlin-3 disrupts the interaction of p53 and MDM2, forcing cells with wildtype p53 to engage cell cycle arrest. p53 KO cells continue to grow in the presence of Nutlin-3 and become enriched in the population over time. From this highly enriched population of p53 KO cells, single cells were cloned and then tested for loss of p53 using western blotting and Sanger sequencing (sequencing primers 5'GCTGGATCCCCACTTTTCCTCT'3 and 5'CATCCCCAGGAGAGATGCTGAG'3).

Assays to measure drug-induced cell death

The FLICK assay was performed as described in Richards et al. 2020[9,25]. Briefly, cells were seeded at a density of 2,000-5,000 cells per well in black 96-well plates (Greiner, #655090). Cells were plated in 90 μL of media and incubated overnight. Cells were then drugged with the indicated doses of drug or vehicle controls, along with 5 μM SYTOX green, in

10 µL media. Dead cell fluorescence was monitored kinetically with a Tecan Spark microplate reader (ex:503, em:524), using a gain that achieved linearity of the SYTOX signal for each cell line. A duplicate plate was lysed at the beginning of the assay by adding 0.1% Triton X-100 (Fisher Scientific, #BP151-100) in PBS to each well, and incubating each plate at 37°C for 2-4 hours. At the end of the experiment, all wells were permeabilized with 0.1% Triton X-100 in PBS. The permeabilized plates were used to determine the total cell number at the assay start and endpoint. Total cell number at intermediate timepoints was inferred using a simple model of exponential growth. The measured dead cell fluorescence and total cell fluorescence was then used to calculate the fluorescence of live cells at each timepoint. From these 3 numbers, all calculations necessary to determine relative viability (RV), fractional viability (FV), and GR value (GR) can be made.

$$RV = \frac{Live_{treated}}{Live_{untreated}} \qquad FV = \frac{Live}{Live + Dead} \qquad GR = 2\text{^}\left(\frac{log_2\left(\frac{Live_{treated}}{Live_{T0}}\right)}{log_2\left(\frac{Live_{untreated}}{Live_{T0}}\right)}\right) - 1$$

Dose response curves and LF kinetic curves were calculated using a custom MATLAB script, as described previously (Richards et al., 2020). Sigmoidal dose response curves were fit using a four-parameter logistic regression to determine the plateau, hill slope, EC_{max}, and EC_{50}. These parameters were determined using least squares regression-based curve fitting in MATLAB. An example is shown below for FV, but the same equation was also used to fit RV and GR.

$$FV(x) = EC_{max} + \frac{FV_0 - EC_{max}}{1 + 10^{((x - EC_{50}) * hill\ slope)}}$$

The previously described lag-exponential death (LED) equation was used to model cell death over time[30]. This model optimizes several parameters, including LF_0 (the starting lethal fraction), LF_p (the death plateau), D_0 (the death onset time), and D_R (the maximum rate of death). The area under the resulting LED curve was also calculated (AUC).

$$LF(t) = LF_0 + \left(LF_p - LF_0\right) * \left(1 - e^{-D_R(t - D_0)}\right)$$

Drug GRADE was calculated as described in Schwartz et al., 2020[28]. FV and GR were calculated as described above, and then FV values were normalized relative to the basal death rate of each cell line. For each drug, the GR and FV from doses where GR ≥ 0 were fit to a line to determine the slope (m_{drug}). The maximum slope that could be observed over the same range of GR values was also determined (m_{max}), and then GRADE was calculated.

$$GRADE = \frac{tan^{-1}\left(m_{drug}\right)}{tan^{-1}(m_{max})}$$

Flow cytometry-based analysis of apoptosis and cell cycle

Cleaved-CASP3 and cleaved-PARP positivity was quantified to monitor activation of apoptosis. At the indicated timepoints, the media was collected from each sample and the remaining adherent cells were trypsinized. The media and trypsinized cells were pooled for each sample, pelleted, and then stained with a 1:1000 dilution of LIVE/DEAD fixable violet stain at room temperature for 30 minutes. Each sample was then washed with cold PBS. Samples were fixed in 4% fresh formaldehyde in PBS at room temperature for 15 minutes. Cells were washed with cold PBS, pelleted, and resuspended in ice-cold 100% methanol. The fixed and permeabilized cells were then stored at -20°C overnight. The methanol was removed the following day, and samples were washed twice with PBS-T (PBS + 0.1% Tween-20). Primary cleaved-CASP3 antibody was diluted 1:500 in 50% PBS-T : 50% Odyssey Blocking Buffer (OBB, LI-COR Odyssey, #927-40010). Samples were then incubated with diluted cleaved-CASP3 antibody at room temperature for 8 hours. After incubation, samples were washed once with PBS-T, and then incubated with cleaved-PARP-647 antibody and goat-anti rabbit Alexa-488. Both antibodies were diluted 1:250 in 50% PBS-T : 50% OBB and incubated overnight at room temperature. Samples were then pelleted, washed twice with PBS-T, resuspended in

PBS-T, and filtered in preparation for flow cytometry analysis. Samples were run on either a BD LSRII or a Miltenyi MACSQuant VYB cytometer with laser and filter settings appropriate for reading LIVE/DEAD violet, Alexa-488, and Alexa-647. Analysis to identify live cells and quantify the number of cleaved-CASP3+/cleaved-PARP+ cells was performed using FlowJo.

For the analysis of cell cycle position, media and adherent cells were collected as described above. Cells were pelleted and then fixed by gentle resuspension in ice-cold 70% ethanol in PBS. Cells were then stored at -20°C overnight. Each sample was then washed twice with PBS, and permeabilized on ice for 15 minutes using Triton x-100 (0.25% in PBS). Permeabilized cells were then rinsed with 1% BSA in PBS. Samples were then incubated overnight at 4°C with phospho-histone H3 antibody, which was diluted 1:100 in 1% BSA. The following day, cells were washed twice with 1% BSA and then incubated with goat-anti rabbit Alexa-488 secondary (in 1% BSA) for 1 hour at room temperature. Cells were then washed once with 1% BSA and once with PBS. Each sample was then resuspended in 10% RNase A in PBS (Sigma-Aldrich, #R6513). Propidium iodide (10mg/ml) was then added to each sample at a final concentration of 0.5mg/ml. Samples were then filtered and analyzed on a BD LSRII. Cell cycle position was quantified using FlowJo analysis software.

Imaging and time-lapsed microscopy

For imaging experiments to monitor apoptotic/non-apoptotic morphologies, U2OS and U2OS^{p53KO} cells were plated in black 96-well plates. Cells were plated at a density of 2,000-5,000 cells per well, depending on the goals of the experiment. Cells were allowed to adhere overnight and then treated with the indicated drugs and 50 nM SYTOX green. Endpoint or time-lapsed images were then collected using either an IncuCyte S3 or an IncuCyte SX5 (Essen Biosciences). Images were collected at 20x magnification in phase, as well as the green channel (ex: 460 ± 20, em: 524 ± 20, acquisition time: 300ms). Images were visualized and analyzed using Fiji (ImageJ2).

Time-lapsed microscopy was also utilized in the STACK assay. Prior to the assay, U2OS-mCherry and U2OS^{p53KO}-mCherry cells were generated. Integration of mCherry into the genome of these cells was achieved using a viral H2B-mCherry plasmid. Cells were then plated and drugged as above. Images were collected on the IncuCyte S3 at 10x magnification in phase, the green channel (ex: 460 ± 20, em: 524 ± 20, acquisition time: 300ms), and the red channel (ex:585 ± 20, em: 635 ± 70, acquisition time: 400ms). The counts per well for the SYTOX+ and mCherry+ objects were then determined using the built-in IncuCyte Software (Essen Biosciences) and exported to excel for analysis using a custom MATLAB script.

RNA-seq of conditioned media and evaluation by GSEA

Conditioned media was generated from U2OS and U2OS^{p53KO} cells, before and after exposure to etoposide. For both genotypes, $1x10^6$ cells were plated on 10 cm plates and incubated overnight. Cells were then treated with either 31.6 μM etoposide or DMSO. After 48 hours of drug or vehicle treatment, the conditioned media was collected and passed through a 0.45 μm filter to remove cellular debris. Each conditioned media was diluted 50:50 with fresh media to replenish growth factors, and then immediately used to treated U2OS cells. The recipient U2OS cells were plated at 300,000 cells/well in a 6-well plate 1 day prior to treatment. A T0 sample was also collected prior to addition of the conditioned media. U2OS cells were exposed to the conditioned media for 8 hours and then trypsinized and flash frozen. Total RNA was extracted using the RNeasy Mini Kit (Qiagen, #74104). The manufacturer's instructions were followed to purify RNA, and then $25x10^6$ million reads were sequenced for each sample. RNA sequences were aligned and counted using the DolphinNext RNA-seq Pipeline[53]. Genes with less than 20 counts were trimmed, and DESeq2's parametric fit was used to calculate the log_2 fold-change (L2FC) and adjusted p-value for each gene. Hits were identified based on both a L2FC ($x<-0.4$ or $x>0.4$) and significance cutoff ($x<0.05$). GSEA was run with a pre-ranked list of the L2FC values to determine pathway-level enrichments.

Simulation of population-level responses to DNA damage in the presence and absence of p53

The response of cells to DNA damage was modeled as a biphasic response. For untreated cells, growth is modeled simply as an exponential growth equation (equation I). For cells treated with DNA damage, the change in population size is modeled with exponential equations for growth and death (equation II). To simulate a dose curve of treated p53 WT cells, the modeled growth rate was gradually decreased to 0, and then the death rate was gradually increased. The drug-induced death rate was parameterized around experimentally observed values. Importantly, cell death was only set to occur in cells that had completely growth arrested. To simulate how loss of cell cycle arrest would affect the population size, treated cells were allowed to grow at their normal rate, but maintained their p53 WT death rates. Loss of cell death was simulated by setting the death rate to 0.

I. $Cells_{live} = \left(Cells_{T0} * 2^{\wedge\left(\frac{t}{\tau c}\right)}\right)$ II. $Cells_{live} = \left(Cells_{T0} * 2^{\wedge\left(\frac{t}{\tau d}\right)}\right) - \left(Cells_{T0} * 2^{\wedge\left(\frac{t}{\tau d}\right)} * D_R\right)$

Chemo-genetic profiling of responses to DNA damage in the presence and absence of p53

Whole-genome CRISPR screens were performed in U2OS and U2OS^{p53KO} cells using the GeCKOv2 two-vector system (Addgene, #1000000049). The two pooled DNA half-libraries (A and B) were combined to generate a library of 123,411 sgRNAs. This library was amplified according to the Zhang lab's protocol (available on Addgene) and virus was generated using 293T cells. U2OS-Cas9 and U2OS^{p53KO}-Cas9 cells were generated using viral transduction of the lentiCas9-Blast plasmid (Addgene, #52962), followed by a 5-day selection with 5 µg/mL blasticidin. U2OS-Cas9 and U2OS^{p53KO}-Cas9 cells were transduced with the GeCKOv2 viral

library using a “spinfection”. For each genotype, >200 x10^6 cells were spinfected to achieve a total library coverage of 300-500x. To perform the spinfection, 2x10^6 cells were combined with 300 µL of virus and 0.8 µL/mL polybrene (Millipore, #TR1003G) in the well of a 12-well plate (final volume of 2 mL). This volume of virus was selected experimentally to achieve a final MOI of 0.3. The 12-well plate was then centrifuged at 37°C for 2 hours at 830 x g. The media was gently replaced after the spin and cells were allowed to recover overnight. The following day, cells were replated into 8-layer flasks (Greiner Bio-one, #678108). Cells were incubated overnight and then treated with 1 µg/mL puromycin for 3 days. After the 3-day puromycin treatment the cells were replated into 8-layer flasks and further expanded for 3 days. On day -1 of the drug screen, 50-100 x10^6 cells (~400 – 800x coverage) were plated in triplicate for each of the experimental conditions. For each genotype, 50 x10^6 cells were also saved in triplicate for the T0 controls. On day 0, the treated conditions were drugged with 5 µM etoposide. Untreated cells were passaged on days 1 and 3 (maintaining 400x coverage), and treated cells were passaged on day 3. Live cells from the treated and untreated conditions were all collected and frozen on day 4. Genomic DNA was isolated from the cell pellets using a phenol-chloroform–based extraction method, and sgRNA sequences were extracted from each genome by PCR (forward: 5’CGATTTCTTGGCTTTATATATCTTGTGG’3 and reverse: 5’CTCTGCTGTCCCTGTAATAAACC’3). A second round of PCR was used to add multiplexing barcodes, and each gel-purified library was sequenced on a HiSeq4000 at 300x coverage.

Analysis of chemo-genetic profiles using relative population size (L2FC)

The read quality of the sequences from the chemo-genetic screen were verified using FastQC, and then the libraries were de-multiplexed using the barcode splitter function in the FASTX tool kit. The FASTX trimmer function was used to remove the non-variable sgRNA regions from each sequence. Reads were mapped to the GeCKOv2 library using Bowtie2, allowing for a single mismatch. Guides with low counts were trimmed by removing the bottom

5% of sgRNAs. miRNA sequences were also removed. Sequencing depth was normalized using the distribution of the 1000 non-targeting guides. For each comparison of interest (untreated/T0 and treated/untreated for each genotype), the $\log_2$ fold-change (L2FC) was calculated using a parametric fit in DESeq2. The GeCKOv2 library contains 6 sgRNAs for each of 19,050 genes. These 6 guide-level scores were collapsed to a single gene-level L2FC by taking the mean. The non-targeting sgRNAs were randomized and assigned to 6-guide non-targeting "genes". Each fold-change value was then z-scored based on the distribution of L2FC scores for the non-targeting genes. An empiric p-value was determined for each gene, and this score was FDR corrected using the Benjamini-Hochberg procedure

Death-rate based analysis of chemo-genetic profiles

This rate-based analysis method depends on the comparison of multiple orthogonal measurements to infer the relative contribution of growth inhibition and cell death to the observed L2FC. First, a simple model is generated to simulate the predicted number of cells of each genotype at the end of a CRISPR screening assay, under all possible combinations of varied growth rate and death rate. This model is parameterized around the observed growth and death rates of wild-type U2OS cells (Figure 3C). The result of this simulation is used to generate a phase diagram that highlights the relationship between the traditional fold-change-based screen output (L2FC) and the underlying combination of growth rate and death rate (Figure 4B). The second measurement that is required for this analysis is the experimentally observed gene-level L2FC. The L2FC for etoposide/untreated and untreated/T0 was computed as described above. Multiple combinations of growth rates and death rates will produce the same L2FC in the etoposide vs. untreated condition (Supplemental Figure 5B). To identify which combination of growth and death rates generated the observed L2FC, the growth rate of each SGKO is experimentally determined by comparing the untreated cells to the T0 input sample. As shown in Supplemental Figure 5C, a high-confidence inference of the drug-induced death rate for each

knockout clone can then be generated from the combination of three features: 1) the relative population size at assay endpoint for each sgRNA in the treated vs. untreated populations, 2) the observed relative growth fitness for each sgRNA based on the untreated vs. T0 comparison, and 3) the experimentally observed coordination between growth and death as measured using GRADE-based analysis. This procedure was used to determine the relative growth rate and relative drug-induced death rate of each sgRNA. Similar to the procedure for calculating L2FC, the 6 guide-level scores for each gene were collapsed by taking the mean. To generate a p-value, the gene-level growth and death rates were z-scored based on the distribution of rates for the non-targeting genes. The z-scored values were bootstrapped to determine an empiric p-value and FDR corrected.

Screen validation

The chemo-genetic CRISPR screen and our rate-based analysis were validated in p53 wildtype cells treated with etoposide. This validation effort included the top and bottom 10 genes from the fold-change based analysis, the top and bottom 10 genes from the death-rate based analysis, and 4 genes involved in the canonical repair of etoposide-induced DNA damage. For each gene, the highest-scoring sgRNA was selected from the GeCKOv2 library. Each guide was cloned into the pX330-puro plasmid. Cloning was performed using the single-step digestion-ligation protocol from the Zhang lab (available on the Zhang lab Addgene page). To validate each guide, U2OS cells were plated in 6-well plates at a density of 200,000 cells per well. Lipofectamine 3000 (Thermo Fisher Scientific, #L3000008) was used to transiently transfect each sgRNA-pX330-puro plasmid into a separate well. Cells were treated with 1 μg/mL puromycin for 3 days after the transfection. Cells were replated at the end of the antibiotic selection and allowed to recover for 2 days. Post-recovery, each pool of single gene knockouts (SGKOs) was plated at 2,000 cells per well on black 96-well plates. Changes in drug sensitivity and growth rate were then measured using FLICK. For measurement of death rate, cells were

treated with 5 μM etoposide for 4 days. The drug sensitivity of each SGKO pool was determined by comparing the LF of each sgRNA to that of a non-targeting sgRNA control (ΔLF) at 96 hours. Non-targeting values across 4 separate experiments were averaged for robustness. Fisher's exact tests were used to evaluate the performance of the fold-change and rate-based analysis methods. For measurement of growth rate, plates of untreated cells were lysed at 24, 48, and 72 hours with 0.1% Triton X-100. The total cell number at each timepoint was fit to an exponential model of growth to determine the growth rate of the non-targeting controls and the SGKO pools.

Cobalt-calcein assay for mPTP opening

The stains used in the mPTP assay (calcein, cobalt (II) chloride hexahydrate, and MitoTracker Red) were obtained from the Image-iT LIVE Mitochondrial Transition Pore Assay Kit (Thermo Fisher Scientific, #I35103). In preparation for measurement of MPT activation, cells were seeded on round glass coverslips in 12-well plates. Treated wells were seeded at a density of 100,000 cells/well, and untreated cells were seeded at 30,000 cells/well. After overnight adherence, cells were treated with the indicated drugs. Cells were stained with calcein at a timepoint after the onset of cell death (as measured by FLICK). Coverslip-adhered cells were washed with PBS supplemented with 1 mM $CaCl_2$ (PBS-Ca). PBS-Ca containing 0.5 μM calcein and 0.2 μM MitoTracker Red was then added to each sample. Samples were then spiked with 10 mM $CoCl_2$ and mixed by pipetting. Cells were then incubated at 37°C in 5% CO_2 for 15 minutes. Samples were washed twice with PBS-Ca and then submerged in PBS-Ca until imaging. Each glass coverslip was placed on a slide immediately prior to imaging, and all images were taken within 30 minutes of staining. Images were collected on an EVOS FL Auto 2 microscope with a 40x objective using GFP (ex:470, em:510) and Texas Red (ex:585, em:624) light cubes (Life Technologies). Images were analyzed in Fiji (ImageJ2). Each cell was masked

based on its MitoTracker Red signal, and then the mean fluorescence intensity of calcein was determined for each cell. A minimum of 50 cells were counted for each experimental condition.

Data analysis and statistics

Unless otherwise noted, data analysis was performed in MATLAB (version R2019b) using built-in functions. Code for generating dose response curves, death kinetic curves, and GRADE plots in MATLAB is available on GitHub (https://github.com/MJLee-Lab). Violin and beeswarm-style plots were generated in GraphPad Prism 9 (version 9.5.0). Pair-wise statistical comparisons were made using a two-sample Kolmogorov-Smirnov test. For the L2FC, growth rate, and death rate values from the chemo-genetic screens, significance was determined empirically by bootstrapping a p-value and performing FDR correction with the Benjamini-Hochberg procedure. GSEA analyses were performed using the GSEA 4.1.0 package, and the associated data was plotted in MATLAB. ImageStudio v4.0.21 was used to analyze western blots. Flow cytometry analysis was performed using FlowJo version 10.8.1. Image analysis was performed using Fiji (ImageJ2, version 2.3.0).

ACKNOWLEDGEMENTS

We thank current and past members of the UMass Chan Medical School DSB community for their helpful comments and critiques during the design and execution of this study. Additionally, we thank Thomas Leete for his assistance with training in an early stage of this project, Christina Baer for assistance with some microscopy experiments, Amir Mitchell for providing an H2B-mCherry plasmid, Thomas Fazzio for providing the pX330 plasmid, and Michael Green and Dohoon Kim for providing access to some of the cell lines used in this study. This work was supported by grants from the National Institutes of Health/NIGMS (R01 GM127559 to MJL), the NCI (F31 CA268847 to MEH), and the American Cancer Society (RSG-17-011-01 to MJL).

AUTHOR CONTRIBUTIONS

This project was conceived by MEH and MJL. Chemo-genetic screens, siRNA screens, flow cytometry, and cobalt-calcein assays were performed by MEH. Drug sensitivity screens were performed by MEH with assistance from PCG. Cell counting experiments were performed by MEH and REF. Imaging experiments were performed and analyzed by MEH, with assistance from SAP. Evaluation of error between chemo-genetic screen analysis strategies was performed by NWH. MSLI, DAG, and JBS consulted on the design, interpretation, and analysis of assays to interpret mitochondrial function. Meta-analysis of published screens was performed by MJL. All other experiments, statistical analyses, and modeling were conducted by MEH. MEH and MJL wrote and edited the manuscript.

CONFLICTS OF INTEREST

The authors report no conflicting interests.

FIGURE LEGENDS

Figure 1: p53 deletion switches the mechanism of cell death following DNA damage from apoptotic to non-apoptotic. (A) Simplified schematic of the DNA damage response. **(B - C)** DNA damage sensitivity for p53-proficient (WT) and p53-deficient (KO) cell lines. (B) Sensitivity to 9 DNA damaging chemotherapeutic agents in cells with p53 WT or KO cells. Data were generated using the FLICK assay, and scored using the EC_{50} of the relative viability dose response. (C) Chemosensitivity as in (B), from the DepMap drug repurposing dataset. **(D)** Schematic of drug GRADE analysis. **(E)** Example GRADE analysis for U2OS (p53 WT) and A431 (p53 KO) treated with etoposide. Growth rate and death rate data are for the full panel of 10 WT and 10 KO cells in panel B, with rates inferred using GRADE. **(F)** Generation of U2OS^{p53KO} cells. **(G)** Etoposide sensitivity of U2OS and U2OS^{p53KO}. FV measured using FLICK. **(H)** FV EC_{50} for 10 p53 WT cells treated with etoposide in the presence and absence of p53-targeted siRNA. **(I)** Cell death kinetics for U2OS and U2OS^{p53KO} treated with 31.6 μM etoposide. **(J)** As in panel I, but ± zVAD. **(K)** Apoptotic death evaluated using flow cytometry. Example for U2OS treated with etoposide (*left*), quantified (*right*). **(L)** Death morphology in U2OS and U2OS^{p53KO}. Apoptotic “blebbing” morphology shown for U2OS. Non-apoptotic morphology in U2OS^{p53KO}. SYTOX positivity reports loss of membrane integrity. For all panels with error bars, data are mean ± SD from 3 experimental replicates.

Figure 2: Use of alternative death mechanisms in the absence of p53 has been missed due to assay conditions that are insensitive to cell death (A) Etoposide sensitivity for 10 p53 WT and 10 p53 KO cell lines, evaluated using Relative Viability. P-value calculated using KS test. **(B-C)** Simulation of population dynamics following exposure to DNA damage. (B) Population size over time. (C) Simulated RV. For B and C, untreated = black dashed line; DNA

damage with growth arrest and cell death coupled = solid black line; DNA damage inducing only growth arrest = blue line; DNA damage inducing only death = red line.

Figure 3: Genetic screens fail to identify death regulatory proteins due to confounding effects caused by varied growth rates (A) Schematic of pooled screen **(B-C)** Parameterization of drug dose and assay time for pooled screen. Assay length (B) and screen dose (C) were selected to produce intermediate levels of lethality while maintaining a population size large enough for > 300x coverage of the sgRNA library throughout the assay. **(D)** Distribution of all genes compared to core essential genes in the untreated vs. T0 sample. KS test p-value shown. **(E)** GSEA for etoposide vs. untreated samples, showing most enriched gene signatures. Apoptosis is not significant, shown for comparison. **(F)** GSEA-based analysis for 74 published genome-wide screens of apoptotic agents. Apoptotic genes are consistently missed, while screens typically enrich for known proliferation genes. **(G)** Gene-level $\log_2$ fold change (L2FC) for U2OS (WT) compared to U2OS^{p53KO} (KO). DNA repair genes and core essential genes shown to demonstrate enrichment for genes that reduce growth fitness in chemo-genetic profiling data.

Figure 4: Death rate-based analysis accurately identifies genes that regulate drug-induced death (A) Simulation to highlight conceptual issues with common analysis methods. Pooled genetic screens do not score the relationship between WT and KO cells, but instead, the relative abundance of KO cells in treated and untreated populations (L2FC). In the example, KO cells die twice as fast, but this is obscured by their modest 20% growth defect, which creates a large difference in population size in the fast-growing untreated population. In the example, L2FC is positive in spite of a higher death rate in the knockout cells. Positive L2FC (i.e. enrichment) is generally interpreted as drug resistance. **(B)** Full simulation for all combinations

of growth rates and death rates. Phase diagram shows how changes to growth/death combine to create population sizes that are commonly interpreted as drug sensitization (Sens.) or drug resistance. **(C)** Error in death rate inferences from L2FC values depending on the growth rate of knockout clones. Absolute error as a function of growth rate (*top*). Phase diagram showing type of error as a function of growth rate and death rate (*bottom*). **(D)** Probability density function (PDF) for non-targeting sgRNAs or DNA repair genes in Untreated vs. T0 comparison. Knockout of DNA repair genes causes reduced growth rate. **(E)** Gene-level chemo-genetic profiling data for etoposide vs. untreated in U2OS cells, projected into phase diagram. DNA repair genes and non-targeting sgRNAs highlighted. **(F-J)** Validation of screen. **(F)** Example validation of TDP2, a DNA repair gene. **(G)** Expanded validation of 40 genes that score strongly by death rate or fold change analysis. **(H)** Validation results for 40 genes compared to predictions based on the death rate-based analysis ($\log_2$ death rate, L2DR) **(I)** As in panel H, but compared to L2FC. For panels H and I, odds ratio (OR) and p-values shown based on one-tailed Fisher's exact test (i.e. hypergeometic distribution). **(J)** Fisher's exact test for the subset of gene knockouts within the validation set with reduced growth rates.

Figure 5: DNA damage activates a respiration-dependent form of necrotic death in the absence of p53. (A) Gene-level $\log_2$ death rate (L2DR) for U2OS (WT) compared to U2OS^{p53KO} (KO). TDP2, p53, and p21 are highlighted to demonstrate directionality of known controls. **(B)** Pathway-level enrichment (GSEA) of apoptotic genes from U2OS and U2OS^{p53KO} chemo-genetic screens analyzed with a fold-change or rate-based analysis. Apoptotic genes are enriched only in U2OS, analyzed using L2DR. **(C)** GSEA for the death rate of etoposide treated cells, showing signatures most enriched in U2OS^{p53KO} cells. Negative normalized enrichment scores (NES) indicate a decrease in death rate, positive NES indicates an increase in death rate. **(D)** Running enrichment score for the oxidative phosphorylation (OXPHOS) signature in U2OS^{p53KO}. **(E)** L2DR for U2OS and U2OS^{p53KO} cells, highlighting OXPHOS genes and known

regulators of MPT-dependent necrosis. **(F)** U2OS and U2OS^{p53KO} cells treated with 31.6 μM etoposide, zVAD, and the indicated death pathway inhibitor for 48 hours. The death onset time (D_0) of each was z-scored relative to the effect of etoposide and zVAD alone (*left-most group*). **(G)** Schematic of how the cobalt-calcein assay differentiates apoptosis and MPT. **(H - I)** Measurement of calcein signal in U2OS and U2OS^{p53KO} cells treated with 31.6 μM etoposide for 36 hours. (H) Quantification of calcein signal in >50 individual cells. (I) Representative images of treated and untreated cells. MitoTracker Red was used to mask and quantify calcein fluorescence.

SUPPLEMENTAL FIGURE LEGENDS

Supplemental Figure 1: Relative viability and drug GRADE across p53-proficient and p53-deficient cell lines. Related to Figure 1. (A) Schematic of the FLICK assay and equations for calculating relative viability (RV), fractional viability (FV), and GR values. (B - C) Sensitivity of p53 WT and p53 KO cell lines to DNA-damaging chemotherapeutics, as measured by (B) RV or (C) drug GRADE.

Supplemental Figure 2: p53 deletion compromises cell cycle arrest but does not prevent activation of DNA repair or BH3 mimetic-induced apoptosis. Related to Figure 1 and Figure 2. (A) Measurement of cell cycle position using PI staining and the mitotic marker pH-H3. Example for untreated U2OS cells (*left*), and quantification of cell cycle phase from cells treated with nutlin (*right*). (B) Kinetic western showing the phosphorylation of the DNA damage marker H2AX in response to etoposide. (C) Activation of apoptotic death in U2OS and U2OS^{p53KO} cells by the BH3 mimetic ABT-199. (D) Schematic for conditioned media experiment. (E) Volcano plot showing the p-values and L2FCs for U2OS cells treated with conditioned media ($\log_2$(U2OS^{p53KO}/U2OS)). (F) Pathway-level enrichment for conditioned media, highlighting enrichment for inflammatory signatures in cells treated with media conditioned by U2OS^{p53KO} cells. (G) Live cell counts over time for U2OS and U2OS^{p53KO} cells treated with a sub-lethal dose of etoposide.

Supplemental Figure 3: U2OS and U2OS^{p53KO} treated with cell death inhibitors. (A) U2OS and U2OS^{p53KO} cells treated with single inhibitors for 8 common cell death pathways. **(B)** U2OS cells treated with higher-order combinations of 6 cell death inhibitors. p53 WT and p53 KO cells were treated with pairs of inhibitors and monitored kinetically in FLICK.

Supplemental Figure 4: Chemo-genetic screening analysis strategy and replicate correlation. Related to Figure 3. (A - B) U2OS cells treated with etoposide for 12 days. (A) Live cells were counted to determine the growth defect of each dose. (B) Dead and live cells were counted to determine fractional viability at each dose. **(C)** Analysis schematic for calculating L2FC from chemo-genetic screens. **(D)** Example of correlation between counts for two replicates of the same screen condition. **(E)** Example of correlation between gene-level L2FC values for two screen replicates. L2FC is calculated in MATLAB without variance stabilization.

Supplemental Figure 5: Validation of rate-based analysis method for chemo-genetic screen. (A) Drug GRADE for U2OS and U2OS^{p53KO} cells treated with etoposide. Dose selected for the CRISPR screen (5 μM) is highlighted. **(B - C)** Schematic for calculation of drug-induced death rate and growth rate from experimentally observed L2FC values. (B) Phase diagram and scatter to highlight one example L2FC that can be produced from multiple combinations of growth and death rate. (C) Calculation of growth rate and inference of the drug-induced death rate. **(D)** Schematic of method used to validate hits from the whole-genome CRISPR screen. **(E)** Validation data generated using FLICK, black = non-targeting sgRNA, blue = targeted gene. **(F)** Phase diagram and scatter plots highlighting validated genes that have a reduced growth rate and are predicted to induce resistance using L2FC. p-values and odds ratios (OR) calculated using a Fishers exact test.

Supplemental Figure 6: Validation of MPT activation in p53 KO cells. (A) Phase and SYTOX green images of U2OS cells treated with 10 μM cyclosporin A (CsA). **(B)** Lethal fraction of U2OS and U2OS^{p53KO} cells treated with CsA, zVAD, or CsA+zVAD. **(C)** Cobalt-calcein assay performed on 3 p53-deficient cell lines treated with 31.6 μM etoposide for 36 hours.

REFERENCES

1. Chonghaile, T.N., Sarosiek, K.A., Vo, T.T., Ryan, J.A., Tammareddi, A., Moore, V.D.G., Deng, J., Anderson, K.C., Richardson, P., Tai, Y.T., et al. (2011). Pretreatment Mitochondrial Priming Correlates with Clinical Response to Cytotoxic Chemotherapy. Science *334*, 1129–1133. 10.1126/science.1206727.

2. Merino, D., Kelly, G.L., Lessene, G., Wei, A.H., Roberts, A.W., and Strasser, A. (2018). BH3-Mimetic Drugs: Blazing the Trail for New Cancer Medicines. Cancer Cell *34*, 879–891. 10.1016/j.ccell.2018.11.004.

3. Galluzzi, L., Vitale, I., Aaronson, S.A., Abrams, J.M., Adam, D., Agostinis, P., Alnemri, E.S., Altucci, L., Amelio, I., Andrews, D.W., et al. (2018). Molecular mechanisms of cell death: recommendations of the Nomenclature Committee on Cell Death 2018. Cell Death Differ *25*, 1–56. 10.1038/s41418-017-0012-4.

4. Tsvetkov, P., Coy, S., Petrova, B., Dreishpoon, M., Verma, A., Abdusamad, M., Rossen, J., Joesch-Cohen, L., Humeidi, R., Spangler, R.D., et al. (2022). Copper induces cell death by targeting lipoylated TCA cycle proteins. Science *375*, 1254–1261. 10.1126/science.abf0529.

5. Maltese, W.A., and Overmeyer, J.H. (2014). Methuosis Nonapoptotic Cell Death Associated with Vacuolization of Macropinosome and Endosome Compartments. Am J Pathology *184*, 1630–1642. 10.1016/j.ajpath.2014.02.028.

6. Holze, C., Michaudel, C., Mackowiak, C., Haas, D.A., Benda, C., Hubel, P., Pennemann, F.L., Schnepf, D., Wettmarshausen, J., Braun, M., et al. (2018). Oxeiptosis, a ROS-induced caspase-independent apoptosis-like cell-death pathway. Nat Immunol *19*, 130–140. 10.1038/s41590-017-0013-y.

7. Mou, Y., Wang, J., Wu, J., He, D., Zhang, C., Duan, C., and Li, B. (2019). Ferroptosis, a new form of cell death: opportunities and challenges in cancer. J Hematol Oncol *12*, 34. 10.1186/s13045-019-0720-y.

8. Diot, C., García-González, A.P., Vieira, A.F., Walker, M., Honeywell, M., Doyle, H., Ponomarova, O., Rivera, Y., Na, H., Zhang, H., et al. (2022). Bacterial diet modulates tamoxifen-induced death via host fatty acid metabolism. Nat Commun *13*, 5595. 10.1038/s41467-022-33299-5.

9. Richards, R., Schwartz, H.R., Honeywell, M.E., Stewart, M.S., Cruz-Gordillo, P., Joyce, A.J., Landry, B.D., and Lee, M.J. (2020). Drug antagonism and single-agent dominance result from differences in death kinetics. Nat Chem Biol, 1–10. 10.1038/s41589-020-0510-4.

10. Harper, J.W., and Elledge, S.J. (2007). The DNA damage response: ten years after. Mol Cell *28*, 739–745. 10.1016/j.molcel.2007.11.015.

11. Jackson, S.P. (2009). The DNA-damage response: new molecular insights and new approaches to cancer therapy. Biochem Soc T *37*, 483. 10.1042/bst0370483.

12. Purvis, J.E., Karhohs, K.W., Mock, C., Batchelor, E., Loewer, A., and Lahav, G. (2012). p53 Dynamics Control Cell Fate. Science *336*, 1440–1444. 10.1126/science.1218351.

13. Hafner, A., Bulyk, M.L., Jambhekar, A., and Lahav, G. (2019). The multiple mechanisms that regulate p53 activity and cell fate. Nat Rev Mol Cell Bio *20*, 1–12. 10.1038/s41580-019-0110-x.

14. Loewer, A., Batchelor, E., Gaglia, G., and Lahav, G. (2010). Basal Dynamics of p53 Reveal Transcriptionally Attenuated Pulses in Cycling Cells. Cell *142*, 89–100. 10.1016/j.cell.2010.05.031.

15. Purvis, J.E., and Lahav, G. (2013). Encoding and decoding cellular information through signaling dynamics. Cell *152*, 945–956. 10.1016/j.cell.2013.02.005.

16. Lowe, S.W., Bodis, S., McClatchey, A., Remington, L., Ruley, H.E., Fisher, D.E., Housman, D.E., and Jacks, T. (1994). p53 Status and the Efficacy of Cancer Therapy in Vivo. Science *266*, 807–810. 10.1126/science.7973635.

17. Lowe, S.W., Ruley, H.E., Jacks, T., and Housman, D.E. (1993). p53-dependent apoptosis modulates the cytotoxicity of anticancer agents. Cell *74*, 957–967. 10.1016/0092-8674(93)90719-7.

18. Paek, A.L., Liu, J.C., Loewer, A., Forrester, W.C., and Lahav, G. (2016). Cell-to-Cell Variation in p53 Dynamics Leads to Fractional Killing. Cell *165*, 631–642. 10.1016/j.cell.2016.03.025.

19. Cremoux, P. de, Salomon, A.V., Liva, S., Dendale, R., Bouchind'homme, B., Martin, E., Sastre-Garau, X., Magdelenat, H., Fourquet, A., and Soussi, T. (1999). p53 Mutation as a Genetic Trait of Typical Medullary Breast Carcinoma. Jnci J National Cancer Inst *91*, 641–643. 10.1093/jnci/91.7.641.

20. Vincent-Salomon, A., Gruel, N., Lucchesi, C., MacGrogan, G., Dendale, R., Sigal-Zafrani, B., Longy, M., Raynal, V., Pierron, G., Mascarel, I. de, et al. (2007). Identification of typical medullary breast carcinoma as a genomic sub-group of basal-like carcinomas, a heterogeneous new molecular entity. Breast Cancer Res *9*, R24. 10.1186/bcr1666.

21. Tenev, T., Bianchi, K., Darding, M., Broemer, M., Langlais, C., Wallberg, F., Zachariou, A., Lopez, J., Macfarlane, M., Cain, K., et al. (2011). The Ripoptosome, a Signaling Platform that Assembles in Response to Genotoxic Stress and Loss of IAPs. Mol Cell *43*, 1–17. 10.1016/j.molcel.2011.06.006.

22. Guo, J., Xu, B., Han, Q., Zhou, H., Xia, Y., Gong, C., Dai, X., Li, Z., and Wu, G. (2018). Ferroptosis: A Novel Anti-tumor Action for Cisplatin. Cancer Res Treat Official J Korean Cancer Assoc *50*, 445–460. 10.4143/crt.2016.572.

23. Yu, S.-W., Wang, H., Poitras, M.F., Coombs, C., Bowers, W.J., Federoff, H.J., Poirier, G.G., Dawson, T.M., and Dawson, V.L. (2002). Mediation of Poly(ADP-Ribose) Polymerase-1-Dependent Cell Death by Apoptosis-Inducing Factor. Science *297*, 259–263. 10.1126/science.1072221.

24. Hu, B., Jin, C., Li, H.-B., Tong, J., Ouyang, X., Cetinbas, N.M., Zhu, S., Strowig, T., Lam, F.C., Zhao, C., et al. (2016). The DNA-sensing AIM2 inflammasome controls radiation-induced cell death and tissue injury. Science *354*, 765–768. 10.1126/science.aaf7532.

25. Richards, R., Honeywell, M.E., and Lee, M.J. (2021). FLICK: an optimized plate reader-based assay to infer cell death kinetics. Star Protoc *2*, 100327. 10.1016/j.xpro.2021.100327.

26. Hafner, M., Niepel, M., Chung, M., and Sorger, P.K. (2016). Growth rate inhibition metrics correct for confounders in measuring sensitivity to cancer drugs. Nat Methods *13*, 1–11. 10.1038/nmeth.3853.

27. Harris, L.A., Frick, P.L., Garbett, S.P., Hardeman, K.N., Paudel, B.B., Lopez, C.F., Quaranta, V., and Tyson, D.R. (2016). An unbiased metric of antiproliferative drug effect in vitro. Nat Methods *13*, 497–500. 10.1038/nmeth.3852.

28. Schwartz, H.R., Richards, R., Fontana, R.E., Joyce, A.J., Honeywell, M.E., and Lee, M.J. (2020). Drug GRADE: An Integrated Analysis of Population Growth and Cell Death Reveals Drug-Specific and Cancer Subtype-Specific Response Profiles. Cell Reports *31*, 107800. 10.1016/j.celrep.2020.107800.

29. Dixon, S.J., Lemberg, K.M., Lamprecht, M.R., Skouta, R., Zaitsev, E.M., Gleason, C.E., Patel, D.N., Bauer, A.J., Cantley, A.M., Yang, W.S., et al. (2012). Ferroptosis: An Iron-Dependent Form of Nonapoptotic Cell Death. Cell *149*, 1060–1072. 10.1016/j.cell.2012.03.042.

30. Forcina, G.C., Conlon, M., Wells, A., Cao, J.Y., and Dixon, S.J. (2017). Systematic Quantification of Population Cell Death Kinetics in Mammalian Cells. Cell Syst *4*, 1–18. 10.1016/j.cels.2017.05.002.

31. Villunger, A., Michalak, E.M., Coultas, L., Müllauer, F., Böck, G., Ausserlechner, M.J., Adams, J.M., and Strasser, A. (2003). p53- and Drug-Induced Apoptotic Responses Mediated by BH3-Only Proteins Puma and Noxa. Science *302*, 1036–1038. 10.1126/science.1090072.

32. Inde, Z., Forcina, G.C., Denton, K., and Dixon, S.J. (2020). Kinetic Heterogeneity of Cancer Cell Fractional Killing. Cell Reports *32*, 107845. 10.1016/j.celrep.2020.107845.

33. Riegman, M., Sagie, L., Galed, C., Levin, T., Steinberg, N., Dixon, S.J., Wiesner, U., Bradbury, M.S., Niethammer, P., Zaritsky, A., et al. (2020). Ferroptosis occurs through an osmotic mechanism and propagates independently of cell rupture. Nat Cell Biol, 1–7. 10.1038/s41556-020-0565-1.

34. Riegman, M., Bradbury, M.S., and Overholtzer, M. (2019). Population Dynamics in Cell Death: Mechanisms of Propagation. Trends Cancer *5*, 558–568. 10.1016/j.trecan.2019.07.008.

35. Hafner, M., Mills, C.E., Subramanian, K., Chen, C., Chung, M., Boswell, S.A., Everley, R.A., Liu, C., Walmsley, C.S., Juric, D., et al. (2019). Multiomics Profiling Establishes the Polypharmacology of FDA-Approved CDK4/6 Inhibitors and the Potential for Differential Clinical Activity. Cell Chem Biol *26*, 1067-1080.e8. 10.1016/j.chembiol.2019.05.005.

36. Grootjans, S., Berghe, T.V., and Vandenabeele, P. (2017). Initiation and execution mechanisms of necroptosis: an overview. Cell Death Differ *24*, 1184–1195. 10.1038/cdd.2017.65.

37. Przybyla, L., and Gilbert, L.A. (2021). A new era in functional genomics screens. Nat Rev Genet, 1–15. 10.1038/s41576-021-00409-w.

38. Colic, M., and Hart, T. (2019). Chemogenetic interactions in human cancer cells. Comput Struct Biotechnology J *17*, 1318–1325. 10.1016/j.csbj.2019.09.006.

39. Colic, M., Wang, G., Zimmermann, M., Mascall, K., McLaughlin, M., Bertolet, L., Lenoir, W.F., Moffat, J., Angers, S., Durocher, D., et al. (2019). Identifying chemogenetic interactions from CRISPR screens with drugZ. Genome Med *11*, 52. 10.1186/s13073-019-0665-3.

40. Shalem, O., Sanjana, N.E., Hartenian, E., Shi, X., Scott, D.A., Mikkelsen, T.S., Heckl, D., Ebert, B.L., Root, D.E., Doench, J.G., et al. (2014). Genome-scale CRISPR-Cas9 knockout screening in human cells. Science *343*, 84–87. 10.1126/science.1247005.

41. Olivieri, M., Cho, T., Álvarez-Quilón, A., Li, K., Schellenberg, M.J., Zimmermann, M., Hustedt, N., Rossi, S.E., Adam, S., Melo, H., et al. (2020). A Genetic Map of the Response to DNA Damage in Human Cells. Cell *182*, 481-496.e21. 10.1016/j.cell.2020.05.040.

42. Diegmiller, R., Salphati, L., Alicke, B., Wilson, T.R., Stout, T.J., and Hafner, M. (2022). Growth-rate model predicts in vivo tumor response from in vitro data. Cpt Pharmacometrics Syst Pharmacol *11*, 1183–1193. 10.1002/psp4.12836.

43. Hart, T., Chandrashekhar, M., Aregger, M., Steinhart, Z., Brown, K.R., MacLeod, G., Mis, M., Zimmermann, M., Fradet-Turcotte, A., Sun, S., et al. (2015). High-Resolution CRISPR Screens Reveal Fitness Genes and Genotype-Specific Cancer Liabilities. Cell *163*, 1515–1526. 10.1016/j.cell.2015.11.015.

44. Arroyo, J.D., Jourdain, A.A., Calvo, S.E., Ballarano, C.A., Doench, J.G., Root, D.E., and Mootha, V.K. (2016). A Genome-wide CRISPR Death Screen Identifies Genes Essential for Oxidative Phosphorylation. Cell Metab *24*, 875–885. 10.1016/j.cmet.2016.08.017.

45. Colville, A., Liu, J.-Y., Thomas, S., Ishak, H.D., Zhou, R., Klein, J.D.D., Morgens, D.W., Goshayeshi, A., Salvi, J.S., Yao, D., et al. (2022). Death-seq identifies regulators of cell death and senolytic therapies. Biorxiv, 2022.04.01.486768. 10.1101/2022.04.01.486768.

46. Schellenberg, M.J., Lieberman, J.A., Herrero-Ruiz, A., Butler, L.R., Williams, J.G., Muñoz-Cabello, A.M., Mueller, G.A., London, R.E., Cortés-Ledesma, F., and Williams, R.S. (2017). ZATT (ZNF451)–mediated resolution of topoisomerase 2 DNA-protein cross-links. Science *357*, 1412–1416. 10.1126/science.aam6468.

47. Tsujimoto, Y., and Shimizu, S. (2007). Role of the mitochondrial membrane permeability transition in cell death. Apoptosis *12*, 835–840. 10.1007/s10495-006-0525-7.

48. Berghe, T.V., Linkermann, A., Jouan-Lanhouet, S., Walczak, H., and Vandenabeele, P. (2014). Regulated necrosis: the expanding network of non-apoptotic cell death pathways. Nat Rev Mol Cell Bio *15*, 135–147. 10.1038/nrm3737.

49. Petronilli, V., Miotto, G., Canton, M., Colonna, R., Bernardi, P., and Lisa, F.D. (1998). Imaging the mitochondrial permeability transition pore in intact cells. Biofactors *8*, 263–272. 10.1002/biof.5520080314.

50. Bonora, M., Morganti, C., Morciano, G., Giorgi, C., Wieckowski, M.R., and Pinton, P. (2016). Comprehensive analysis of mitochondrial permeability transition pore activity in living cells using fluorescence-imaging-based techniques. Nat Protoc *11*, 1067–1080. 10.1038/nprot.2016.064.

51. Sidi, S., Sanda, T., Kennedy, R.D., Hagen, A.T., Jette, C.A., Hoffmans, R., Pascual, J., Imamura, S., Kishi, S., Amatruda, J.F., et al. (2008). Chk1 Suppresses a Caspase-2 Apoptotic Response to DNA Damage that Bypasses p53, Bcl-2, and Caspase-3. Cell *133*, 864–877. 10.1016/j.cell.2008.03.037.

52. Tabe, Y., Sebasigari, D., Jin, L., Rudelius, M., Davies-Hill, T., Miyake, K., Miida, T., Pittaluga, S., and Raffeld, M. (2009). MDM2 Antagonist Nutlin-3 Displays Antiproliferative and Proapoptotic Activity in Mantle Cell Lymphoma. Clin Cancer Res *15*, 933–942. 10.1158/1078-0432.ccr-08-0399.

53. Yukselen, O., Turkyilmaz, O., Ozturk, A.R., Garber, M., and Kucukural, A. (2020). DolphinNext: a distributed data processing platform for high throughput genomics. Bmc Genomics *21*, 310. 10.1186/s12864-020-6714-x.

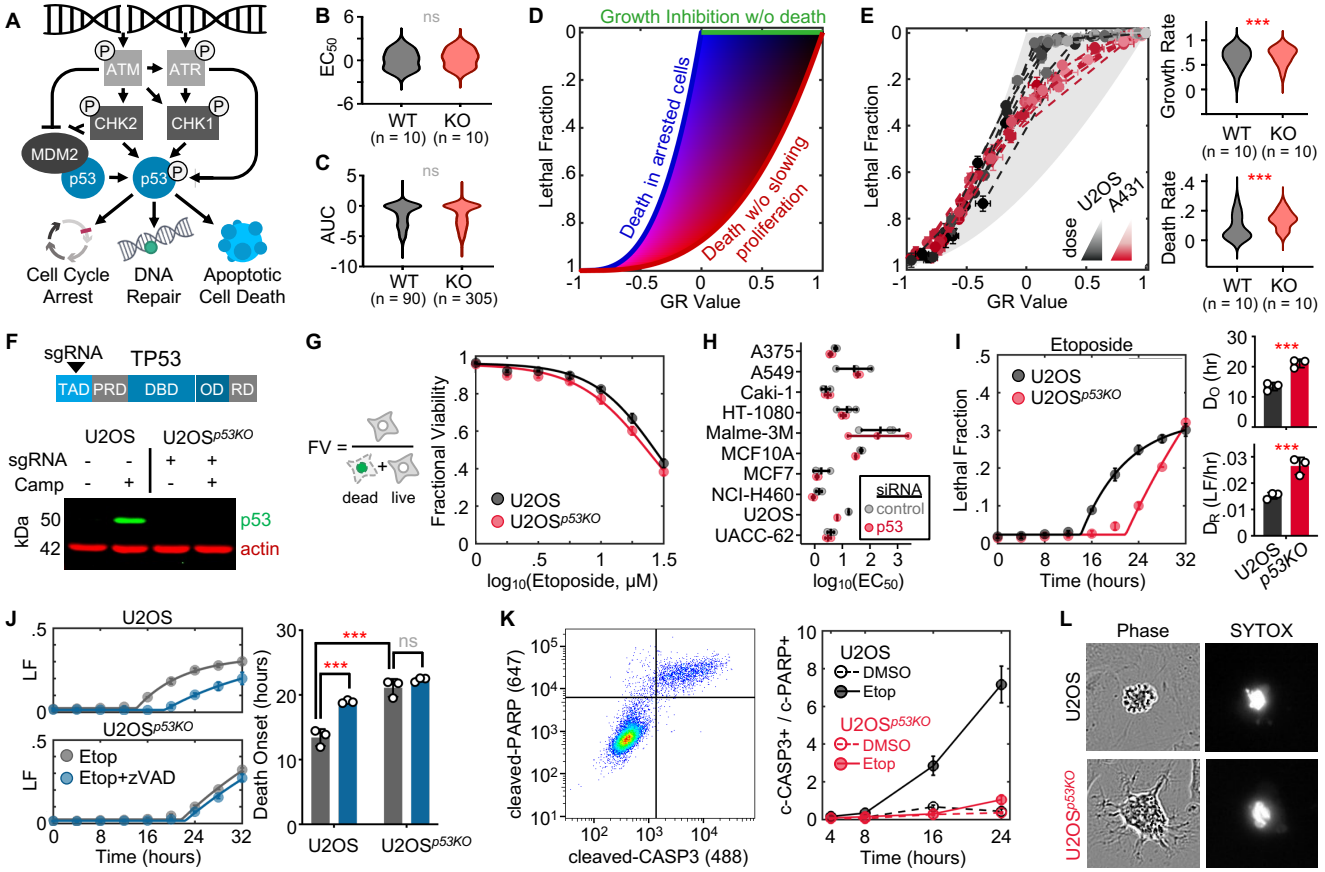

Figure 1: p53 deletion switches the mechanism of cell death following DNA damage from apoptotic to non-apoptotic. (A) Simplified schematic of the DNA damage response. **(B - C)** DNA damage sensitivity for p53-proficient (WT) and p53-deficient (KO) cell lines. (B) Sensitivity to 9 DNA damaging chemotherapeutic agents in cells with p53 WT or KO cells. Data were generated using the FLICK assay, and scored using the EC_{50} of the relative viability dose response. (C) Chemosensitivity as in (B), from the DepMap drug repurposing dataset. **(D)** Schematic of drug GRADE analysis. **(E)** Example GRADE analysis for U2OS (p53 WT) and A431 (p53 KO) treated with etoposide. Growth rate and death rate data are for the full panel of 10 WT and 10 KO cells in panel B, with rates inferred using GRADE. **(F)** Generation of U2OS^{p53KO} cells. **(G)** Etoposide sensitivity of U2OS and U2OS^{p53KO}. FV measured using FLICK. **(H)** FV EC_{50} for 10 p53 WT cells treated with etoposide in the presence and absence of p53-targeted siRNA. **(I)** Cell death kinetics for U2OS and U2OS^{p53KO} treated with 31.6 μM etoposide. **(J)** As in panel I, but ± zVAD. **(K)** Apoptotic death evaluated using flow cytometry. Example for U2OS treated with etoposide (*left*), quantified (*right*). **(L)** Death morphology in U2OS and U2OS^{p53KO}. Apoptotic "blebbing" morphology shown for U2OS. Non-apoptotic morphology in U2OS^{p53KO}. SYTOX positivity reports loss of membrane integrity. For all panels with error bars, data are mean ± SD from 3 experimental replicates.

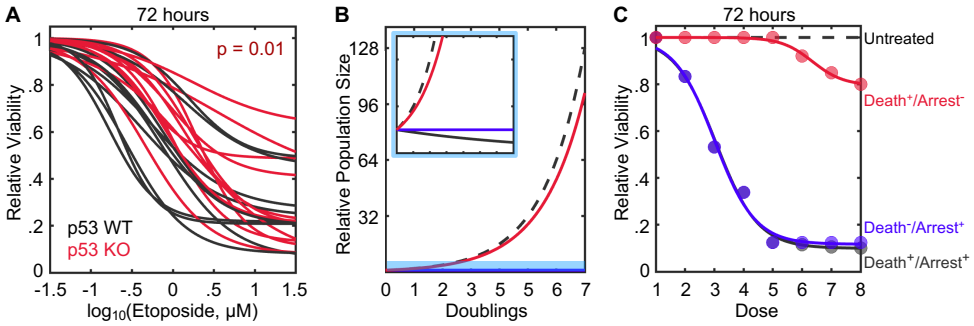

Figure 2: Use of alternative death mechanisms in the absence of p53 has been missed due to assay conditions that are insensitive to cell death (A) Etoposide sensitivity for 10 p53 WT and 10 p53 KO cell lines, evaluated using Relative Viability. P-value calculated using KS test. **(B-C)** Simulation of population dynamics following exposure to DNA damage. (B) Population size over time. (C) Simulated RV. For B and C, untreated = black dashed line; DNA damage with growth arrest and cell death coupled = solid black line; DNA damage inducing only growth arrest = blue line; DNA damage inducing only death = red line.

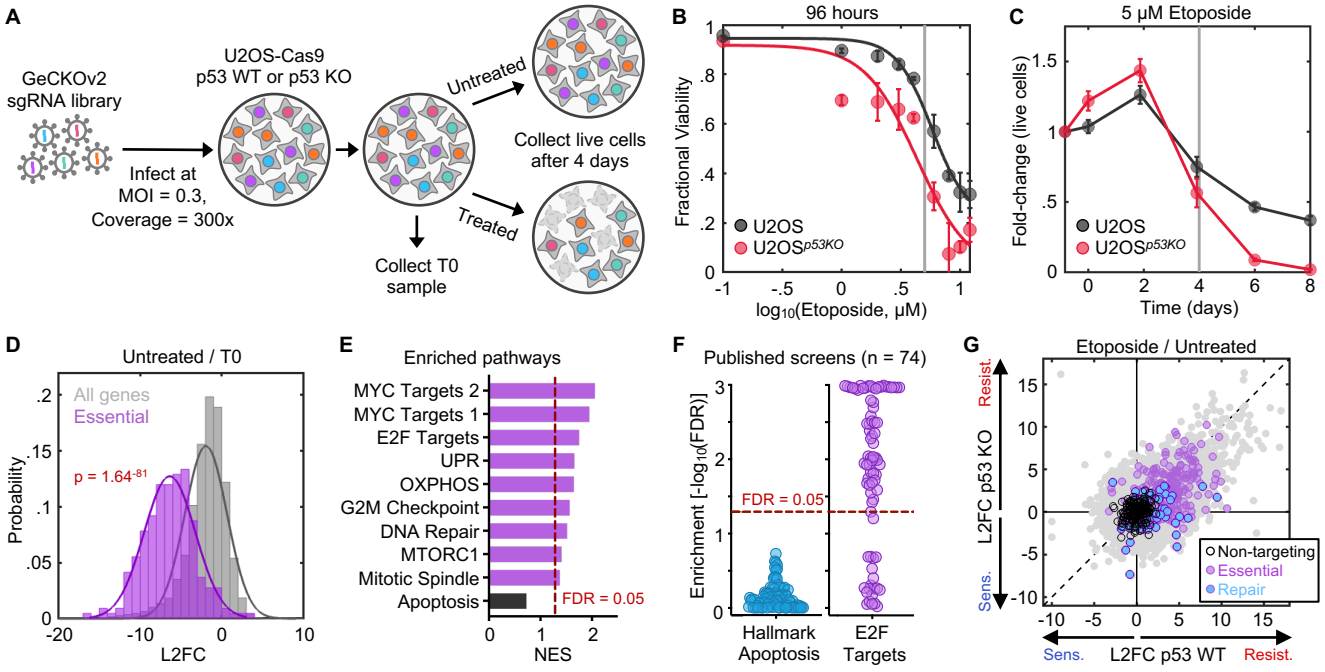

Figure 3: Genetic screens fail to identify death regulatory proteins due to confounding effects caused by varied growth rates (A) Schematic of pooled screen **(B-C)** Parameterization of drug dose and assay time for pooled screen. Assay length (B) and screen dose (C) were selected to produce intermediate levels of lethality while maintaining a population size large enough for > 300x coverage of the sgRNA library throughout the assay. **(D)** Distribution of all genes compared to core essential genes in the untreated vs. T0 sample. KS test p-value shown. **(E)** GSEA for etoposide vs. untreated samples, showing most enriched gene signatures. Apoptosis is not significant, shown for comparison. **(F)** GSEA-based analysis for 74 published genome-wide screens of apoptotic agents. Apoptotic genes are consistently missed, while screens typically enrich for known proliferation genes. **(G)** Gene-level $\log_2$ fold change (L2FC) for U2OS (WT) compared to U2OS^{p53KO} (KO). DNA repair genes and core essential genes shown to demonstrate enrichment for genes that reduce growth fitness in chemo-genetic profiling data.

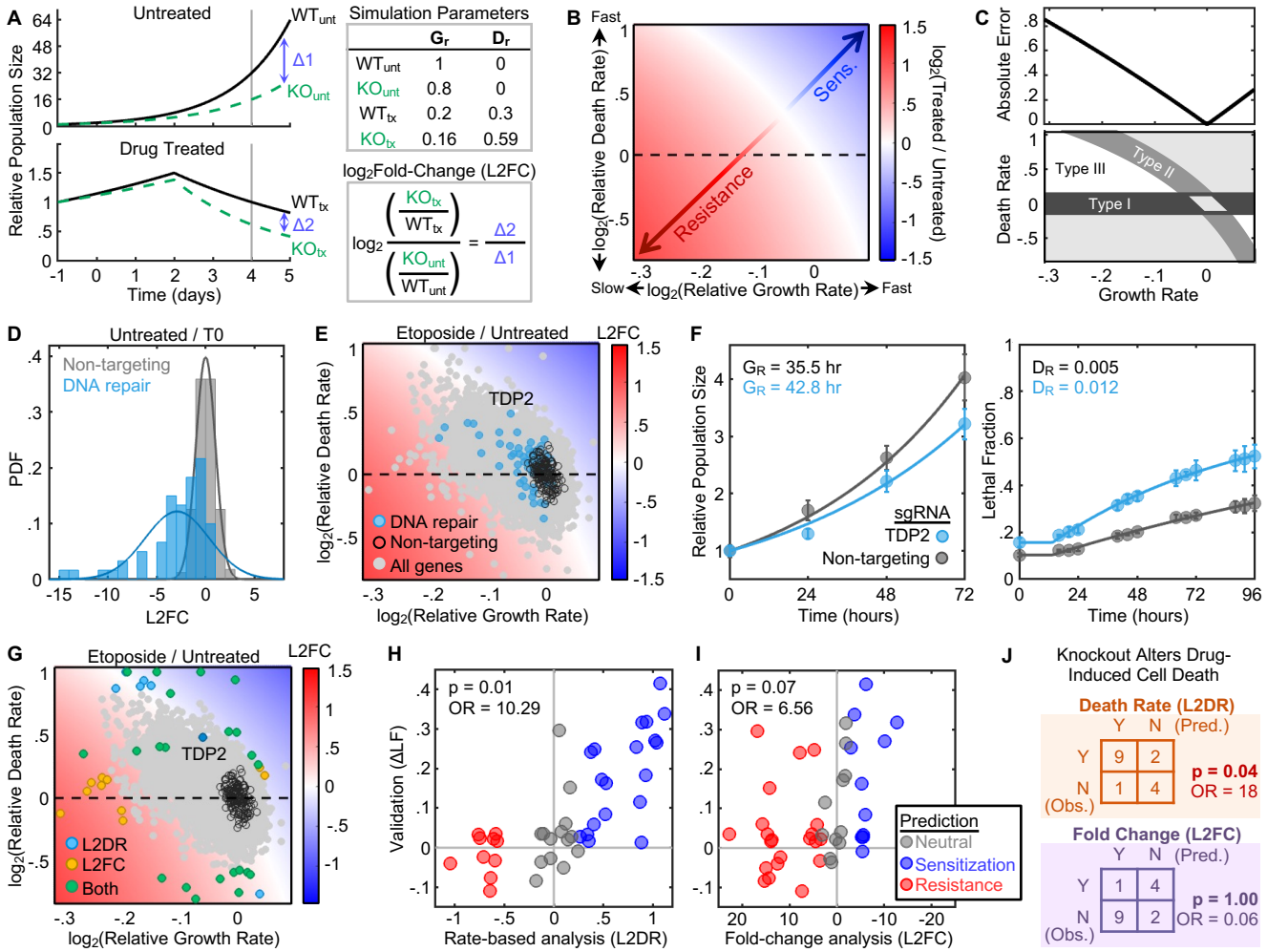

Figure 4: Death rate-based analysis accurately identifies genes that regulate drug-induced death (A) Simulation to highlight conceptual issues with common analysis methods. Pooled genetic screens do not score the relationship between WT and KO cells, but instead, the relative abundance of KO cells in treated and untreated populations (L2FC). In the example, KO cells die twice as fast, but this is obscured by their modest 20% growth defect, which creates a large difference in population size in the fast-growing untreated population. In the example, L2FC is positive in spite of a higher death rate in the knockout cells. Positive L2FC (i.e. enrichment) is generally interpreted as drug resistance. **(B)** Full simulation for all combinations of growth rates and death rates. Phase diagram shows how changes to growth/death combine to create population sizes that are commonly interpreted as drug sensitization (Sens.) or drug resistance. **(C)** Error in death rate inferences from L2FC values depending on the growth rate of knockout clones. Absolute error as a function of growth rate (*top*). Phase diagram showing type of error as a function of growth rate and death rate (*bottom*). **(D)** Probability density function (PDF) for non-targeting sgRNAs or DNA repair genes in Untreated vs. T0 comparison. Knockout of DNA repair genes causes reduced growth rate. **(E)** Gene-level chemo-genetic profiling data for etoposide vs. untreated in U2OS cells, projected into phase diagram. DNA repair genes and non-targeting sgRNAs highlighted. **(F-J)** Validation of screen. **(F)** Example validation of TDP2, a DNA repair gene. **(G)** Expanded validation of 40 genes that score strongly by death rate or fold change analysis. **(H)** Validation results for 40 genes compared to predictions based on the death rate-based analysis ($\log_2$ death rate, L2DR) **(I)** As in panel H, but compared to L2FC. For panels H and I, odds ratio (OR) and p-values shown based on one-tailed Fisher's exact test (i.e. hypergeometic distribution). **(J)** Fisher's exact test for the subset of gene knockouts within the validation set with reduced growth rates.

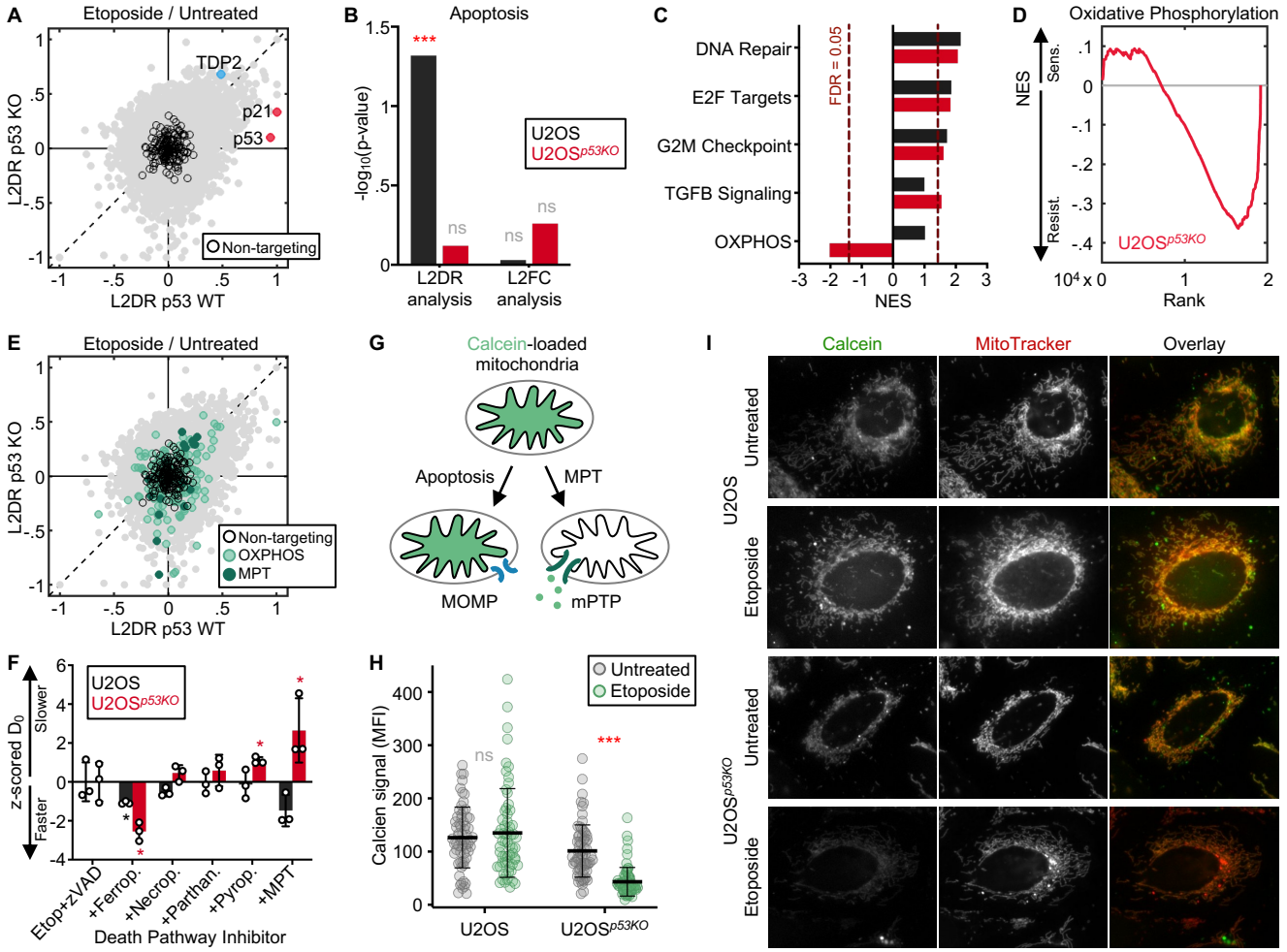

Figure 5: DNA damage activates a respiration-dependent form of necrotic death in the absence of p53. (A) Gene-level $\log_2$ death rate (L2DR) for U2OS (WT) compared to U2OS^{p53KO} (KO). TDP2, p53, and p21 are highlighted to demonstrate directionality of known controls. **(B)** Pathway-level enrichment (GSEA) of apoptotic genes from U2OS and U2OS^{p53KO} chemo-genetic screens analyzed with a fold-change or rate-based analysis. Apoptotic genes are enriched only in U2OS, analyzed using L2DR. **(C)** GSEA for the death rate of etoposide treated cells, showing signatures most enriched in U2OS^{p53KO} cells. Negative normalized enrichment scores (NES) indicate a decrease in death rate, positive NES indicates an increase in death rate. **(D)** Running enrichment score for the oxidative phosphorylation (OXPHOS) signature in U2OS^{p53KO}. **(E)** L2DR for U2OS and U2OS^{p53KO} cells, highlighting OXPHOS genes and known regulators of MPT-dependent necrosis. **(F)** U2OS and U2OS^{p53KO} cells treated with 31.6 μM etoposide, zVAD, and the indicated death pathway inhibitor for 48 hours. The death onset time (D_0) of each was z-scored relative to the effect of etoposide and zVAD alone (*left-most group*). **(G)** Schematic of how the cobalt-calcein assay differentiates apoptosis and MPT. **(H - I)** Measurement of calcein signal in U2OS and U2OS^{p53KO} cells treated with 31.6 μM etoposide for 36 hours. (H) Quantification of calcein signal in >50 individual cells. (I) Representative images of treated and untreated cells. MitoTracker Red was used to mask and quantify calcein fluorescence.

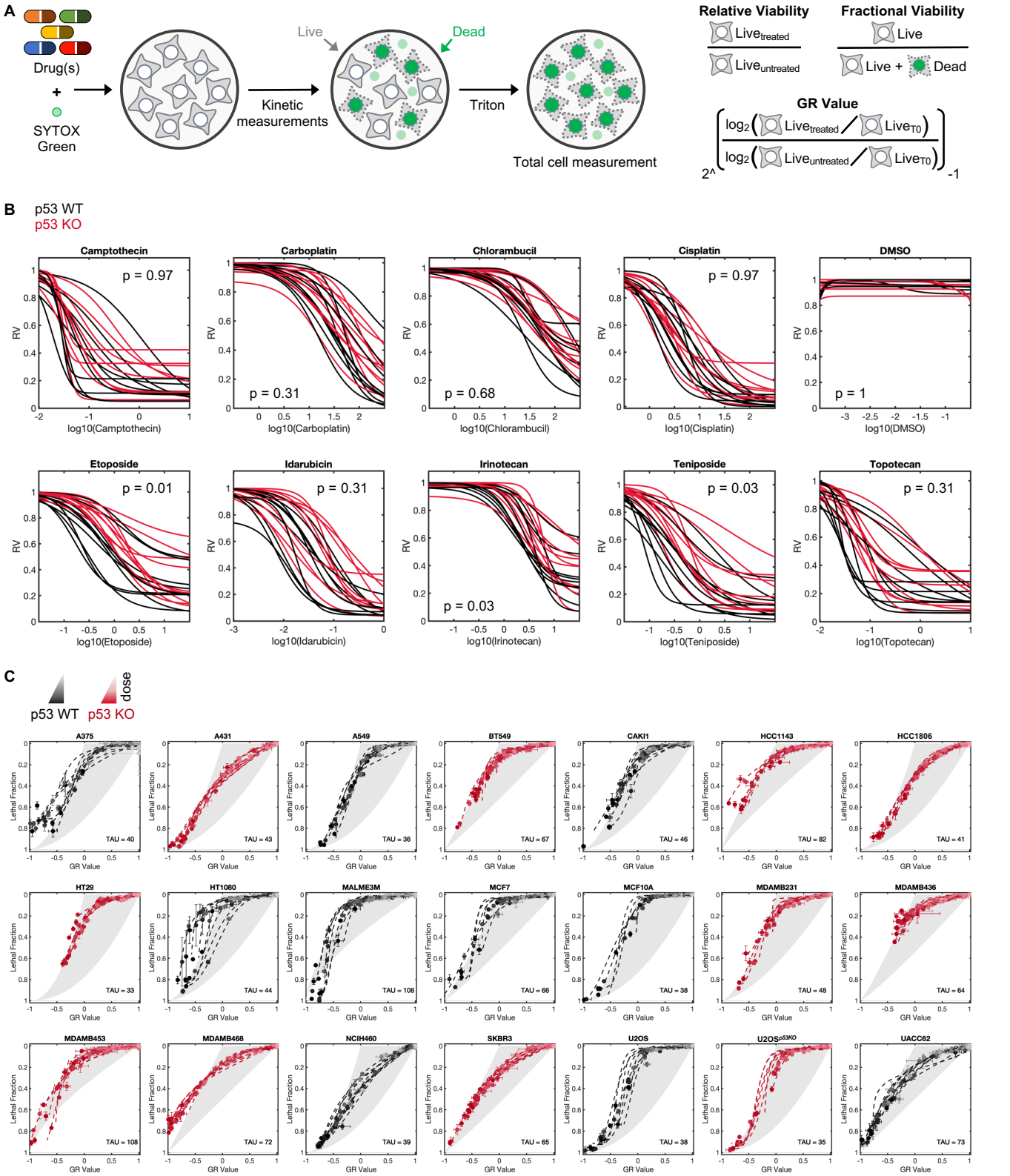

Supplemental Figure 1: Relative viability and drug GRADE across p53-proficient and p53-deficient cell lines. Related to Figure 1. (A) Schematic of the FLICK assay and equations for calculating relative viability (RV), fractional viability (FV), and GR values. **(B - C)** Sensitivity of p53 WT and p53 KO cell lines to DNA-damaging chemotherapeutics, as measured by (B) RV or (C) drug GRADE.

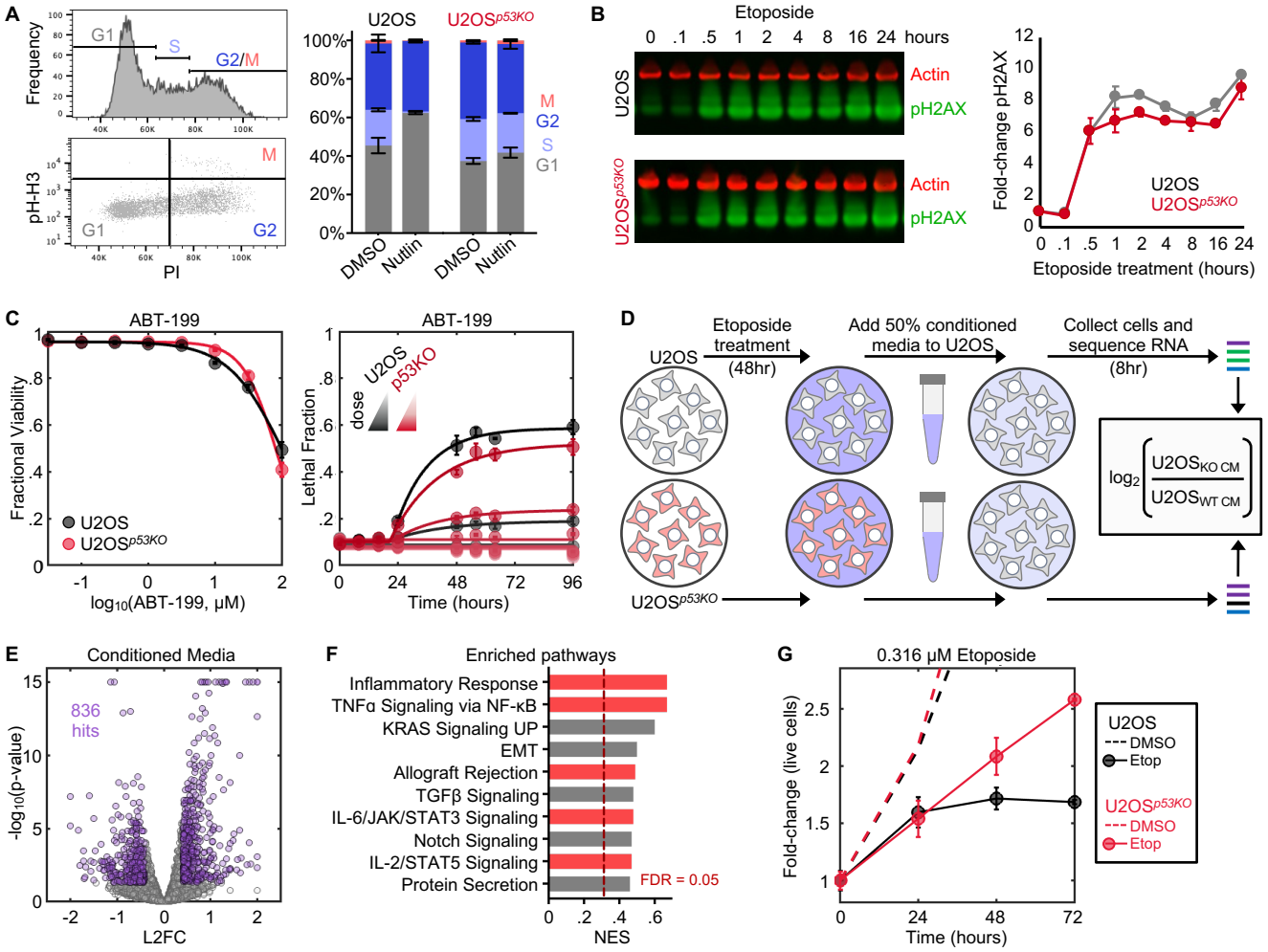

Supplemental Figure 2: p53 deletion compromises cell cycle arrest but does not prevent activation of DNA repair or BH3 mimetic-induced apoptosis. Related to Figure 1 and Figure 2. (A) Measurement of cell cycle position using PI staining and the mitotic marker pH-H3. Example for untreated U2OS cells (*left*), and quantification of cell cycle phase from cells treated with nutlin (*right*). **(B)** Kinetic western showing the phosphorylation of the DNA damage marker H2AX in response to etoposide. **(C)** Activation of apoptotic death in U2OS and U2OS^{p53KO} cells by the BH3 mimetic ABT-199. **(D)** Schematic for conditioned media experiment. **(E)** Volcano plot showing the p-values and L2FCs for U2OS cells treated with conditioned media ($\log_2$(U2OS^{p53KO}/U2OS)). **(F)** Pathway-level enrichment for conditioned media, highlighting enrichment for inflammatory signatures in cells treated with media conditioned by U2OS^{p53KO} cells. **(G)** Live cell counts over time for U2OS and U2OS^{p53KO} cells treated with a sub-lethal dose of etoposide.

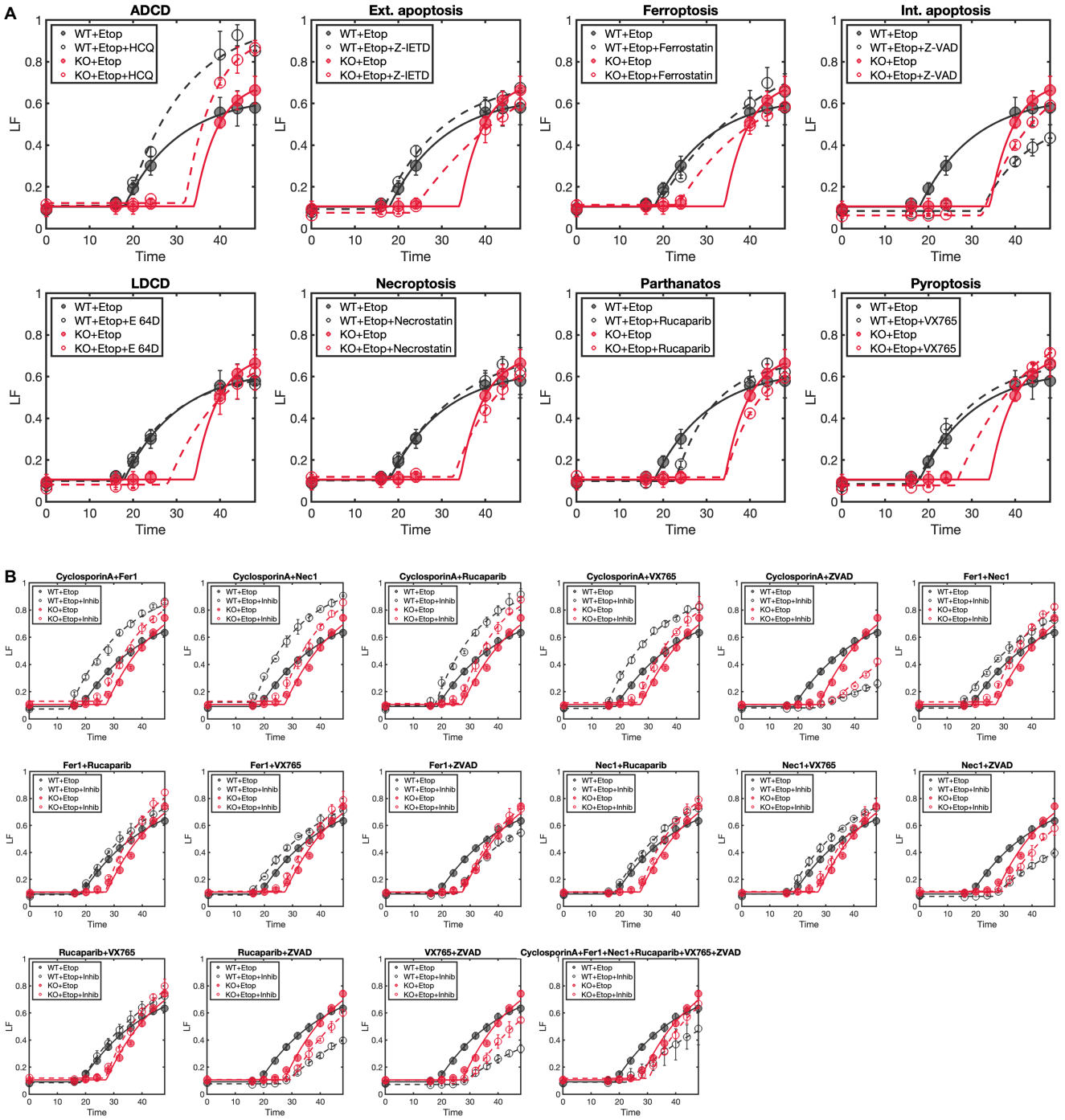

Supplemental Figure 3: U2OS and U2OS^{p53KO} treated with cell death inhibitors. (A) U2OS and U2OS^{p53KO} cells treated with single inhibitors for 8 common cell death pathways. **(B)** U2OS cells treated with higher-order combinations of 6 cell death inhibitors. p53 WT and p53 KO cells were treated with pairs of inhibitors and monitored kinetically in FLICK.

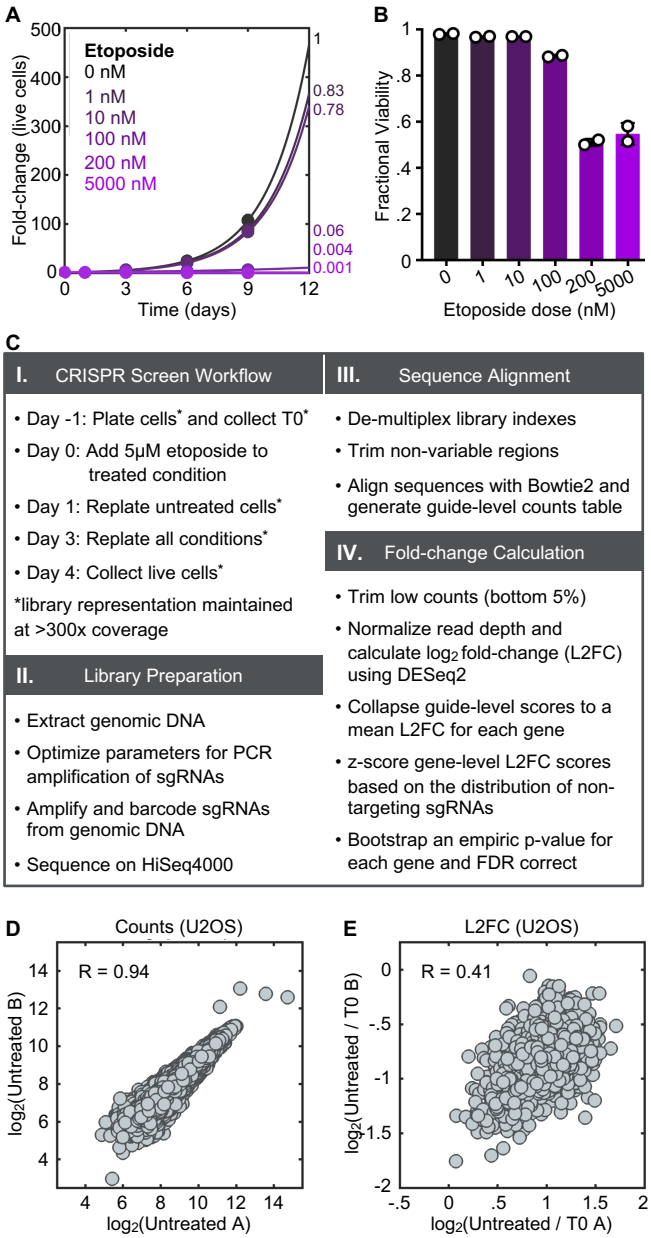

Supplemental Figure 4: Chemo-genetic screening analysis strategy and replicate correlation. Related to Figure 3. (A - B) U2OS cells treated with etoposide for 12 days. (A) Live cells were counted to determine the growth defect of each dose. (B) Dead and live cells were counted to determine fractional viability at each dose. **(C)** Analysis schematic for calculating L2FC from chemo-genetic screens. **(D)** Example of correlation between counts for two replicates of the same screen condition. **(E)** Example of correlation between gene-level L2FC values for two screen replicates. L2FC is calculated in MATLAB without variance stabilization.

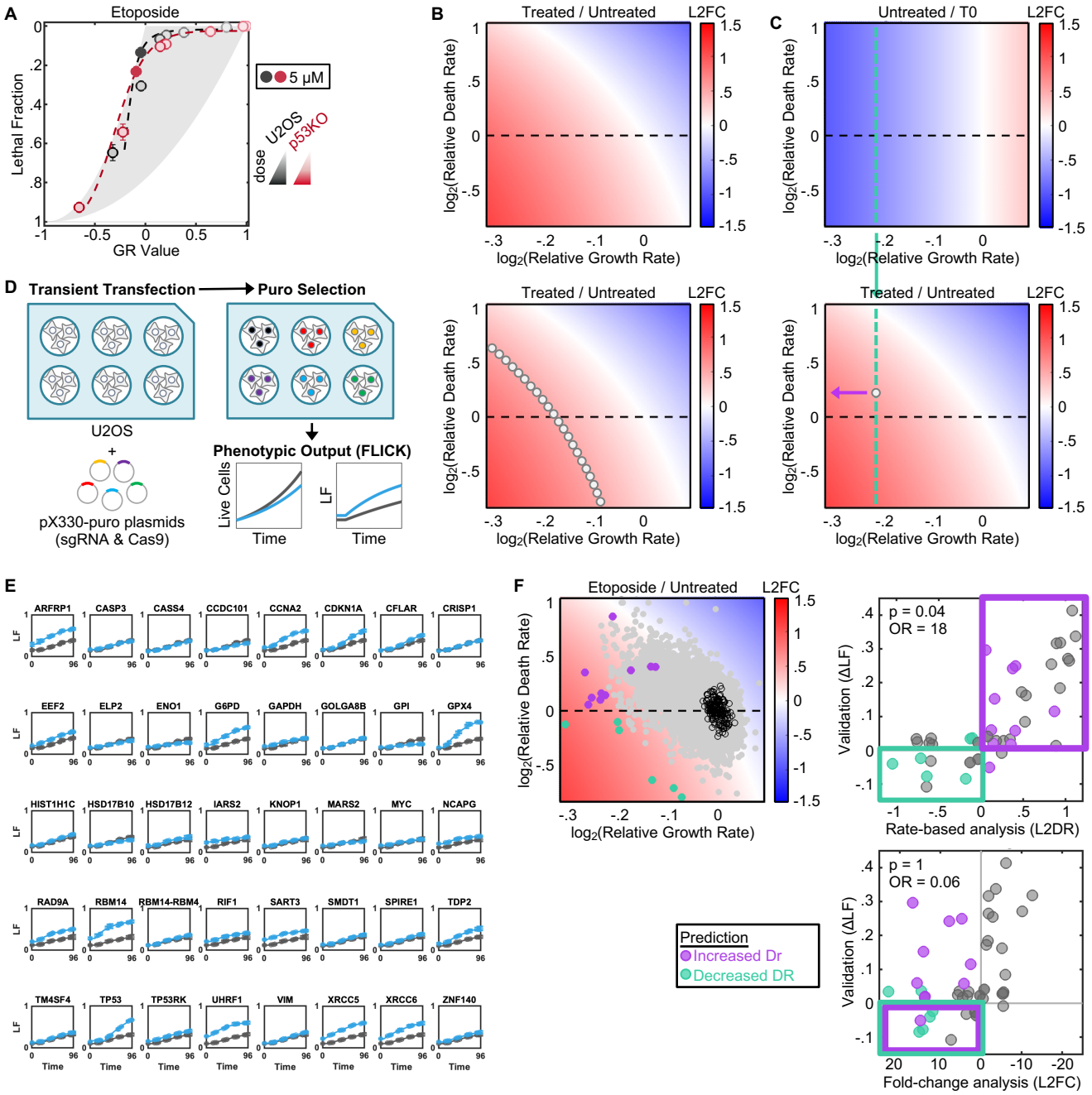

Supplemental Figure 5: Validation of rate-based analysis method for chemo-genetic screen. (A) Drug GRADE for U2OS and U2OS^{p53KO} cells treated with etoposide. Dose selected for the CRISPR screen (5 μM) is highlighted. **(B - C)** Schematic for calculation of drug-induced death rate and growth rate from experimentally observed L2FC values. (B) Phase diagram and scatter to highlight one example L2FC that can be produced from multiple combinations of growth and death rate. (C) Calculation of growth rate and inference of the drug-induced death rate. **(D)** Schematic of method used to validate hits from the whole-genome CRISPR screen. **(E)** Validation data generated using FLICK, black = non-targeting sgRNA, blue = targeted gene. **(F)** Phase diagram and scatter plots highlighting validated genes that have a reduced growth rate and are predicted to induce resistance using L2FC. p-values and odds ratios (OR) calculated using a Fishers exact test.

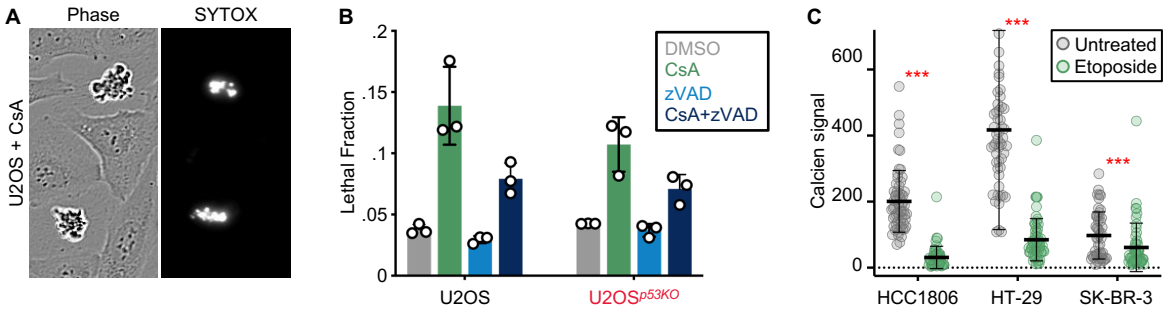

Supplemental Figure 6: Validation of MPT activation in p53 KO cells. (A) Phase and SYTOX green images of U2OS cells treated with 10 μM cyclosporin A (CsA). **(B)** Lethal fraction of U2OS and U2OS^{p53KO} cells treated with CsA, zVAD, or CsA+zVAD. **(C)** Cobalt-calcein assay performed on 3 p53-deficient cell lines treated with 31.6 μM etoposide for 36 hours.